University of Nottingham
UK | CHINA | MALAYSIA

Department of Mechanical, Materials and Manufacturing Engineering

Design and Manufacture of a Carbon Fibre Wheel Rim: Manufacturing Constraints, Structural Validation and Comparison to Aluminium For Formula Student

Author: Alex Hartshorn

Student ID: 20488121

Course: Mechanical Engineering

Date of report: 5th May 2026

Supervisor: Dr Surojit Sen

Summary

Formula Student challenges university teams to design, manufacture and race a single-seat electric vehicle. For the University of Nottingham Racing team, reducing vehicle mass is a direct route to improving acceleration, braking and cornering performance. The wheel rim is a particularly important target because it contributes to both unsprung mass and rotational inertia. This means any mass saving has a greater effect than the same reduction on a static part of the chassis. This project therefore focused on the design, manufacture and validation of a carbon fibre reinforced polymer wheel rim to replace the team's existing aluminium rim.

The aim of the project was to develop a lightweight composite wheel that remained compatible with the Formula Student vehicle package, met relevant tyre and rim geometry requirements, and could be structurally validated against representative load cases and SAE J3204 based test conditions. The work flowed from requirement definition and concept selection, followed by CAD embodiment, composite finite element analysis using ANSYS ACP, tooling design, prepreg manufacture, inspection and physical validation.

Two main development iterations were completed. The first prototype established the manufacturing route, generated physical test data for comparison with simulation, and exposed key limitations in dimensional compliance, manufacturability, and ETRTO geometric compliance. These findings then informed targeted design refinements and a strengthened validation approach, including dimensional inspection, ultrasonic, CT scanning, and mechanical testing, offering a level of validation that is rarely achieved in Formula Student.

The final CFRP rim achieved a mass reduction of approximately 56 percent compared with the aluminium baseline. Vehicle simulation predicted a sprint lap time improvement of 0.26 seconds, equivalent to approximately 9.26 Formula Student points. The project therefore demonstrates not only a significant performance gain, but also a repeatable design, manufacture and validation framework for structural composite components within a student racing environment.

Future work should focus on fatigue testing, full track validation and applying the developed methodology to a future 10-inch wheel platform.

Contents

Nomenclature

Symbol	Quantity	Unit
E_1	In-plane stiffness (fibre direction)	GPa
E_2	In-plane stiffness (transverse direction)	GPa
G_{12}	In-plane shear modulus	GPa
ν_{12}	Major Poisson's ratio	–
I	Second moment of area / rotational inertia	$kg \cdot m^2$
m	Mass	kg
R	Radius	m
SF	Safety factor	–
σ	Stress	MPa
ε	Strain	–

Acronyms

Acronym	Meaning
ACP	ANSYS Composite PrepPost
CAD	Computer Aided Design
CFRP	Carbon Fibre Reinforced Polymer
CLT	Classical Laminate Theory
CMM	Coordinate Measuring Machine
CT	Computed Tomography
CTE	Coefficient of Thermal Expansion
ETRTO	European Tyre and Rim Technical Organisation
FE	Finite Element
FEA	Finite Element Analysis
FS	Formula Student
FSG	Formula Student Germany
FSUK	Formula Student United Kingdom
IMU	Inertial Measurement Unit
IPG	Developer of CarMaker vehicle simulation software
LTS	Lap Time Simulation
MGU	Motor Gearbox Unit
NDT	Non Destructive Testing
PCD	Pitch Circle Diameter
PMI	Polymethacrylimide Foam Core
SAE	Society of Automotive Engineers
TIR	Total Indicated Runout
UD	Unidirectional Fibre
UoNR	University of Nottingham Racing
UT	Ultrasonic Testing

1. Introduction

1.1. Formula Student

Every year, UoNRacing (the University of Nottingham racing team) competes in Formula Student, one of the largest engineering competitions in the world. The event is a multidisciplinary challenge in which student teams design and build a Formula-style single-seater race car. Teams score points not only through the car's dynamic performance across multiple events, but also through how effectively the vehicle has been engineered in terms of safety, cost, business viability, and overall performance.

Figure 1 - FS24/25 Car presented at the team's annual car launch

UoN Racing manufactures most of its car in-house, ensuring students develop competence across both design and manufacture. While this increases project complexity, it strengthens quality control and improves design feedback. Furthermore, as the team continues to climb the world rankings, the design strategy has increasingly shifted from commercially available components to bespoke, custom-designed parts, increasing the need for design and manufacturing expertise.

Figure 2 - UoNRacing at Formula Student UK (Silverstone)

1.2. Vehicle Dynamics

Vehicle performance is governed not only by the driver, but fundamentally by tyre grip, vehicle mass, and available power. With competition regulations limiting power to 80kW [1], the most effective routes to lower lap time are increasing usable grip and reducing mass. This is particularly true for unsprung mass, which is not supported by the suspension springs [2]. This includes the wheels and tyres, uprights, brake assemblies, and - within the team's architecture - outboard drivetrain elements such as the motor and gearbox. These elements are shown in figures 3, 4 and 5.

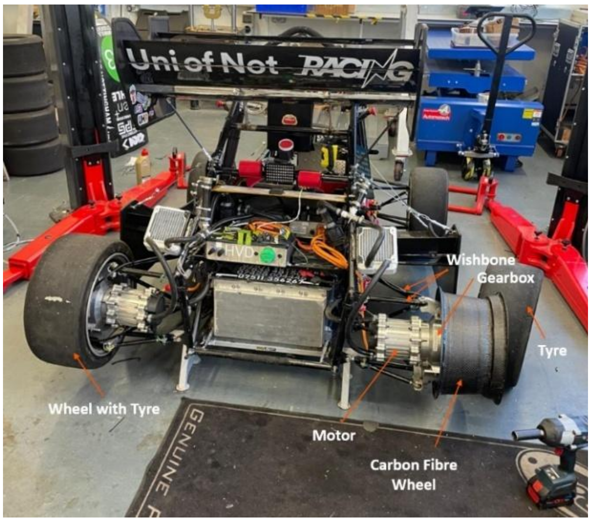

Figure 3 - Rear of vehicle with unsprung components

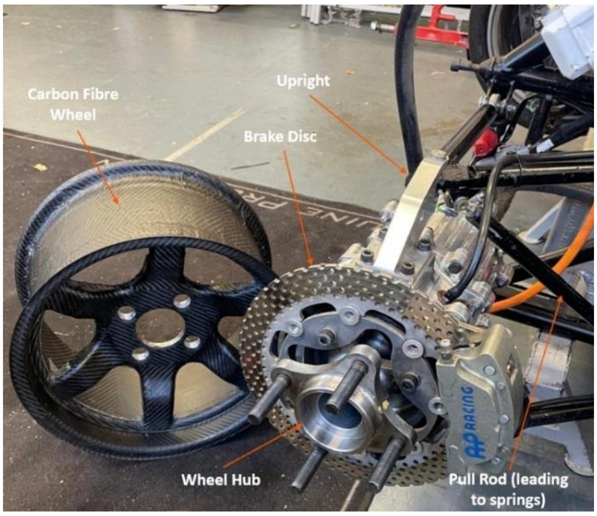

Figure 4 - Rear corner with carbon fibre wheel removed showing rotational and unsprung mass

Reducing unsprung mass improves the suspension's ability to maintain consistent tyre contact over bumps, increasing effective grip and improving control and responsiveness. The suspension must allow the wheel to move upward while the spring and damper then act to return it toward the road surface, maintaining tyre contact, and therefore grip. Since the required force scales with mass, a heavier unsprung assembly generates larger inertial forces for the same bump input. This makes it harder for the damper to control wheel motion and increases the likelihood of reduced contact over disturbances [3]. Reducing unsprung mass lowers these inertial forces, allowing the suspension to track the surface more effectively.

In addition to being unsprung, wheel-and-tyre mass is also rotating. It must be accelerated and decelerated in rotation, and it is also turned during steering inputs. Reducing mass in this rotating assembly lowers the energy required to spin the wheels, allowing faster changes in wheel speed and improved vehicle responsiveness. The reduction in rotational inertia also reduces the steering torque required to rotate the wheels during cornering, contributing to more immediate driver feedback.

These combined effects mean that removing mass from the rotating assembly is often disproportionately beneficial; applying effective mass, a common rule-of-thumb is that 1kg saved at the wheel can be several times more effective than 1kg removed from the sprung chassis. As the tyre cannot realistically be lightweighted, this project focuses on reducing wheel mass as the most effective route to performance gains, the assembly mass distribution can be seen in table 1.

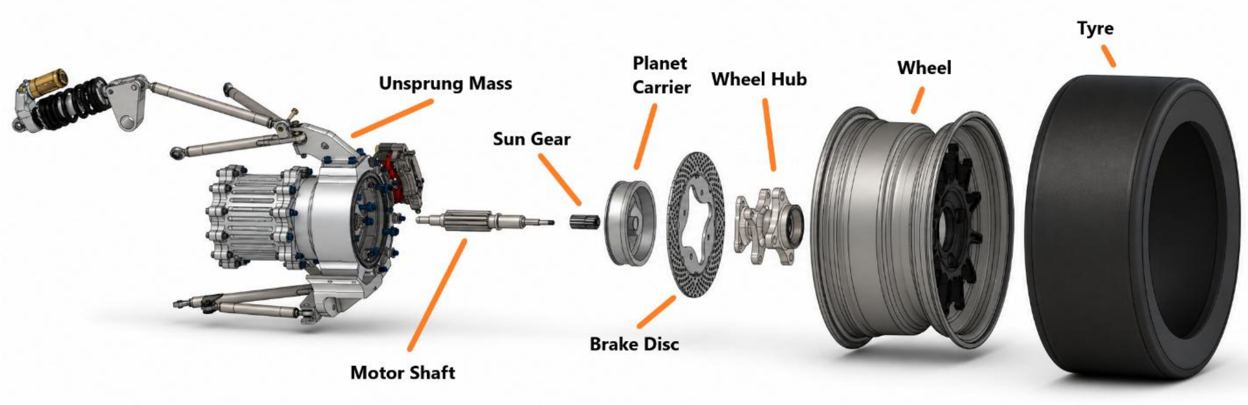

Figure 5 - Rear corner assembly exploded view with rotating components labelled

Table 1 - mass distribution of rear corner in terms of rotational mass

Component	***Unsprung Mass***	***Rotational Mass***	***Motor Shaft***	***Sun Gear***	***Planet Carrier***	***Brake Disc***	***Wheel Hub***	***Wheel Rim***	***Slick Tyre***
Mass / kg	22.52	10.11	0.239	0.042	0.45	0.538	1.513	3.482	3.852

1.3. Material Selection

Lightweighting can be achieved primarily through material selection. This involves choosing materials with higher specific strength, enabling stress requirements to be met without incurring a density (and therefore mass) penalty.

A secondary target is wheel stiffness; this is critical to vehicle dynamics. During cornering, braking and combined loading, excessive rim deflection can alter camber and toe at the contact patch, reducing grip and disrupting the intended suspension behaviour. The wheel must therefore provide high stiffness at low mass, ensuring contact patch control remains dominated by the suspension, rather than rim deformation.

Material selection therefore required a material with high specific strength and high specific stiffness, as the wheel must withstand peak loads while maintaining geometry under load. To screen candidate material families against these competing requirements, an Ashby chart of specific stiffness (E/ρ) versus specific strength (σ/ρ) was used. Materials in the upper-right offer the best combination of stiffness and strength per unit mass, and are therefore desired.

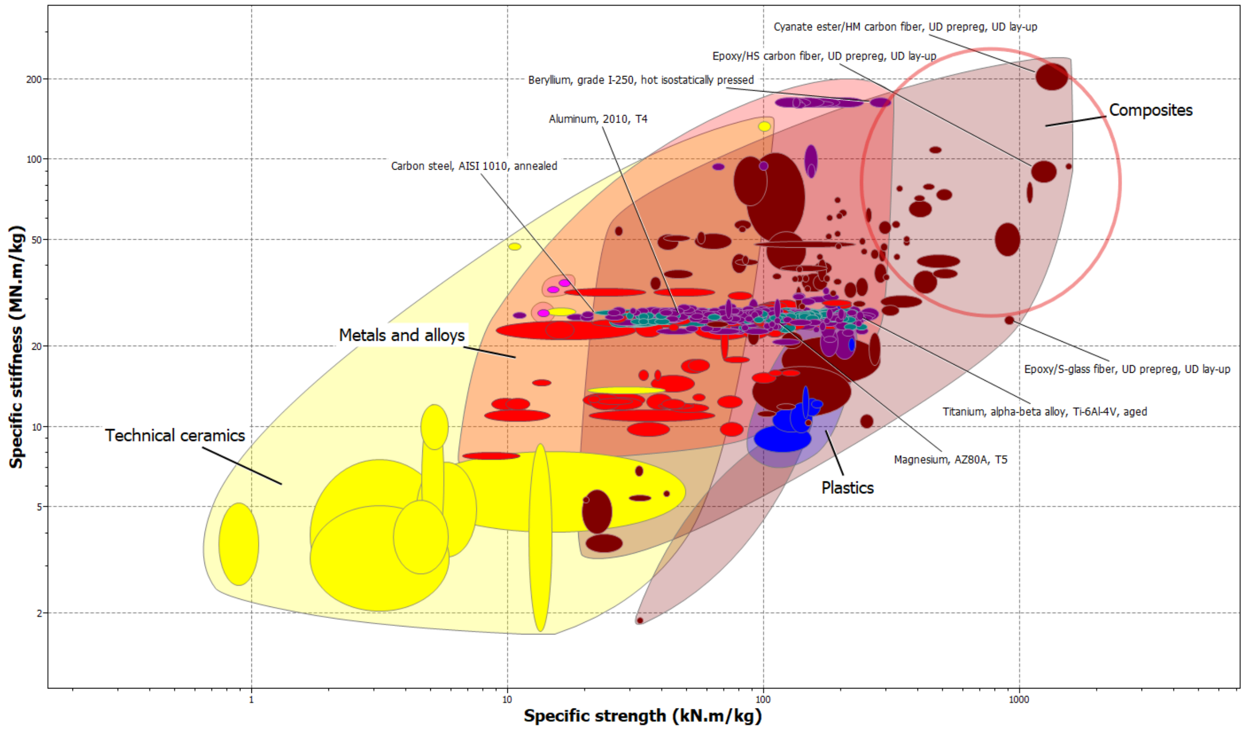

Figure 6 - Specific stiffness (MN.m/kg) to specific strength (kN.m/kg) Ashby chart showing composites offering the highest potential, highlighted in red

A clear hierarchy emerges across the chart. Plastics and technical ceramics sit at the low-performance end for this application. Metals and alloys form a central band; within this, steels and common aluminium alloys are comparatively less favourable, whereas magnesium and titanium move closer to the desired region. However, the composites domain extends furthest into the upper-right of the chart, indicating the strongest combined potential.

The composite region spans multiple resin systems (e.g., epoxy and cyanate ester), but the key outcome is consistent; carbon fibre composites offer the most compelling potential for stiffness and weight criticality.

1.4. Wheels

UoNRacing currently uses aluminium-alloy wheels. While aluminium offers a clear advantage over steel, the current wheel assembly remains a significant contributor to unsprung and rotating mass weighing 3.482kg.

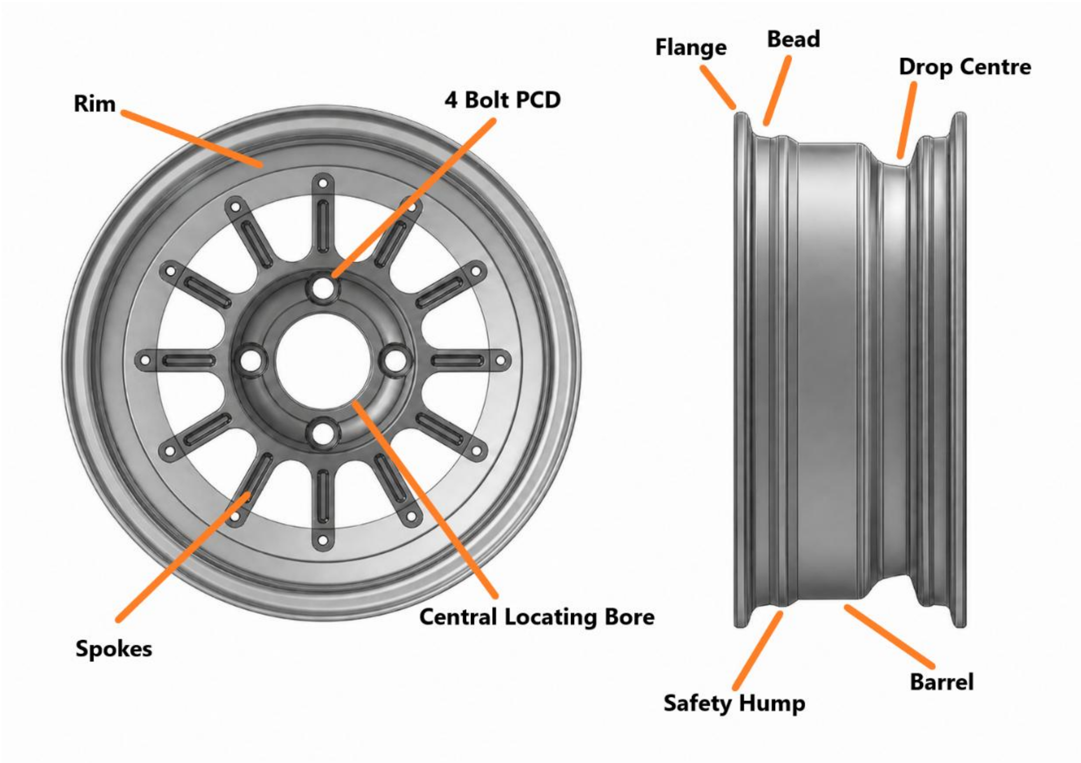

Figure 7 - baseline aluminium rim diagram

A review of commercially available motorsport wheel technologies (Table 2) indicates substantial scope for improvement. Composite rims demonstrate the potential to reduce rim mass by ~2 kg per wheel (approximately 60%) relative to the current configuration. However, these off-the-shelf rims are not compatible with the team's custom wheel hub interface. The difference can be seen in figure 8 and 9 below.

Table 2 - Commercially available wheel rims for Formula Student application [4]

	Current UoNRacing Aluminium Rims (Baseline)	*OZ Racing Magnesium 13"*	*OZ Racing Hybrid Carbon CL 13"*
Image			
Weight	3.482kg	~2.45kg	~1.4kg
Stiffness	Low	High	Very High
Rotational inertia	High	Medium	Low
Cost per wheel	~£200	~£450	~£650
Mounting	4 Bolt PCD	Centre-lock	Centre-lock

This constraint creates a clear opportunity for in-house development to achieve comparable mass and inertia reductions, thereby improving acceleration, braking, and transient handling.

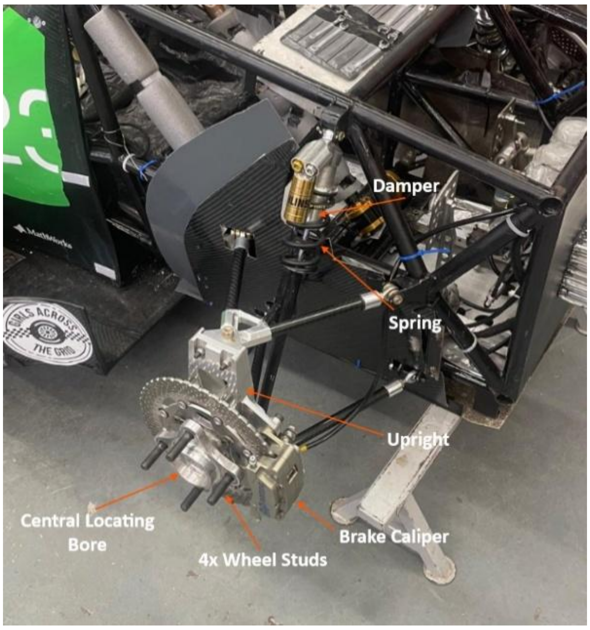

Figure 8 - 2024 front suspension assembly with the wheel removed

Figure 9 - Centre Locking assembly

This motivates the design and development of a set of 13-inch composite wheel rims for the 2025/26 racing season. The project will design, manufacture, test, validate and iterate composite wheels, focusing on achieving meaningful reductions in mass and inertia without compromising stiffness, safety, manufacturability, or reliability.

1.5. Aim and Objectives

To design, manufacture and validate a fully compliant 13-inch carbon fibre wheel rim for the University of Nottingham Racing team, delivering a quantified performance benefit over the aluminium baseline, while establishing a repeatable "first-article" process for future development.

Objectives

- Deliver an FSUK-compliant 13-inch rim design that satisfies the key structural and geometric constraints, including ETRTO rim/tyre interface and vehicle mounting requirements.
- Quantify expected performance gains by achieving target reductions in mass and rotational inertia relative to the baseline.
- Build and correlate an FEA model, demonstrating agreement between simulation results and representative physical testing.
- Strengthen compliance and traceability by producing a controlled artifact/requirements sheet linking each requirement to its supporting evidence.
- Complete validation through a full suite of physical tests and non-destructive testing.

- Produce fully traceable documentation covering requirements, design decisions, manufacturing, inspection, and validation, forming a roadmap for continued performance development.

2. Literature Review

2.1. Composite fundamentals, laminate behaviour, and damage

Composite structures are attractive in performance vehicles because they offer high specific stiffness and strength, enabling mass reduction while maintaining structural capability. However, unlike isotropic metals, composite performance is governed by laminate architecture, ply orientation, and manufacturing quality; consequently, failure is often driven by local material behaviour rather than gross geometry. Across composite aerospace structures, common damage modes include matrix cracking, fibre fracture, interlaminar delamination, and adhesive/interface failure, with damage accumulation under cyclic loading producing progressive stiffness degradation prior to ultimate failure[4].This multi-mode behaviour is particularly relevant for wheel rims because they experience repeated combined loads (radial, cornering and torque) and contain geometric discontinuities (spoke–rim transitions, bead seats, insert interfaces) where local stress states can trigger damage initiation.

Fatigue is therefore not only a life problem but also a functional stiffness-retention problem. Experimental literature on composite rim-type structures reports that fatigue loading can reduce stiffness and encourage crack growth, especially when bending and shear components are present[5, 6]. This motivates an approach in which early analytical laminate sizing is complemented by detailed stress analysis and validation planning, rather than relying on static strength margins alone.

2.2. Composite wheels and Formula Student context

Composite wheels provide a disproportionate performance benefit because mass reduction acts on both unsprung mass and rotational inertia. Lower unsprung mass improves suspension tracking and tyre contact stability, while lower inertia reduces the torque required to accelerate and decelerate the rotating assembly, improving transient response under braking and traction [Wehage]. In Formula Student (FS), such benefits are particularly valuable because event performance is dominated by short transients and frequent direction changes; studies considering FS vehicle performance similarly highlight the importance of transient dynamics and the advantages of reducing unsprung/rotating mass where feasible[7].

However, wheel success in FS depends on reliability as much as peak performance. Evidence from FS design practice indicates that failures often stem from manufacturability oversights, poor tolerancing, weak assembly planning and incomplete test coverage, rather than material choice alone[8, 9]. For composite wheels specifically, the load path is strongly governed by local details such as insert design, interface bonding and bead geometry, making “small” integration choices structurally significant [10, 11]. These findings justify a literature review that links composite damage behaviour to wheel-specific hotspots and to a validation-led engineering workflow.

2.3. Finite element analysis for composite wheel assessment

Finite element (FE) analysis is widely used to assess wheel structures because wheel geometry and load introduction generate highly non-uniform stress states that are difficult to capture analytically. In composite wheels, FE enables resolution of local stresses at spoke–rim transitions, bead seats and insert interfaces, and provides stiffness predictions that can guide laminate and geometry iteration[10, 11]. Practical modelling guidance emphasises that credibility depends on verification steps such as mesh sensitivity, careful contact definition, and realistic representation of constraint conditions, particularly where bolted/clamped interfaces or bonded inserts exist [ANSYS].

Composite modelling also requires attention to what the output will be used for. If the goal is first-order stiffness and stress ranking, linear orthotropic laminate modelling may be sufficient. If the goal is assessing durability or damage tolerance, then fatigue and defect sensitivity become important, since stiffness reduction can precede visible fracture and govern functional performance [5, 6].Literature on wheel fatigue and structural response reinforces that cyclic loading and imperfections can shift hotspot locations and accelerate degradation, which supports using FE as part of an iterative process rather than a single “pass/fail” simulation[5].

2.4. Load case derivation using vehicle dynamics and tyre behaviour

A defensible FE assessment requires load cases derived from vehicle dynamics rather than arbitrary static forces. Under cornering, lateral acceleration produces load transfer from the inside to the outside wheels; quasi-static equilibrium relationships using mass, centre of gravity height and track width provide first-order estimates of wheel normal loads under lateral acceleration[7]. Braking and traction introduce longitudinal forces and drive/brake torques, which combine with vertical and lateral loads to generate multi-axial demand at the hub and through the rim section. These combined load states are essential for capturing realistic stress superposition at insert regions and spoke roots.

Tyre compliance influences the translation of vehicle forces into wheel boundary conditions. Tyre stiffness and force–slip characteristics affect load distribution and the effective constraint at the bead seat and contact patch; representing this behaviour (even with simplified stiffness assumptions) improves realism when applying boundary conditions in FE [Continental]. For FS-type operating regimes, wheel load cases are also shaped by rules and performance envelopes. For example, the FSUK electric power limitation provides a traceable basis for bounding traction capability and supporting assumptions used in longitudinal load estimation[1]. By linking rules-constrained performance, vehicle dynamics load transfer and tyre behaviour, the resulting load cases become traceable and defensible inputs for simulation.

2.5. Validation mindset and the role of inspection (CT and ultrasonics)

Digital predictions ultimately require validation because composite performance is sensitive to manufacturing variability, defects and interface quality. Wheel and rim studies commonly validate FE models using controlled loading where strain or displacement is measured at critical locations and compared to predictions, improving confidence in modelling assumptions before laminate optimisation is pursued [12, 13]. Where fatigue performance is important, stiffness monitoring before and after cycling is frequently used as a functional indicator of damage accumulation [5, 6].

Inspection supports this validation chain by identifying manufacturing defects and in-service damage that may not be externally visible. In composite practice, CT scanning is valuable for volumetric features (porosity, voiding, thickness variation), while ultrasonic methods are effective for planar discontinuities such as delamination and disbonds. Industry-facing guidance highlights that inspection should be tied to expected defect types and failure mechanisms, rather than treated as a generic "quality step" [14]. For composite wheels, this implies targeting inspection around known hotspots (spoke–rim transitions, bead seats and insert interfaces) and using inspection evidence to interpret test scatter and refine modelling assumptions.

3. Methodology

Six wheels were manufactured across two design generations following a structured development cycle progressing from requirements definition through design, manufacture and validation.

Throughout the project, six wheels were produced. While the methodology was refined over time, the core development cycle remained consistent, enabling iterative improvement and convergence towards the final design. Two generations of geometry were designed and manufactured, each producing three wheel variations of the given generation, seen in figure 10 below.

Figure 10 - All 6 of the wheel rims, Version 1 in the foreground

The flow chart in figure 11 illustrates the full development cycle for each iteration, from initial requirements through FEA, manufacture and physical validation, and shows how the feedback loop was closed. Decision gates and verification steps are embedded throughout the process, ensuring each stage is checked against the design requirements before progression.

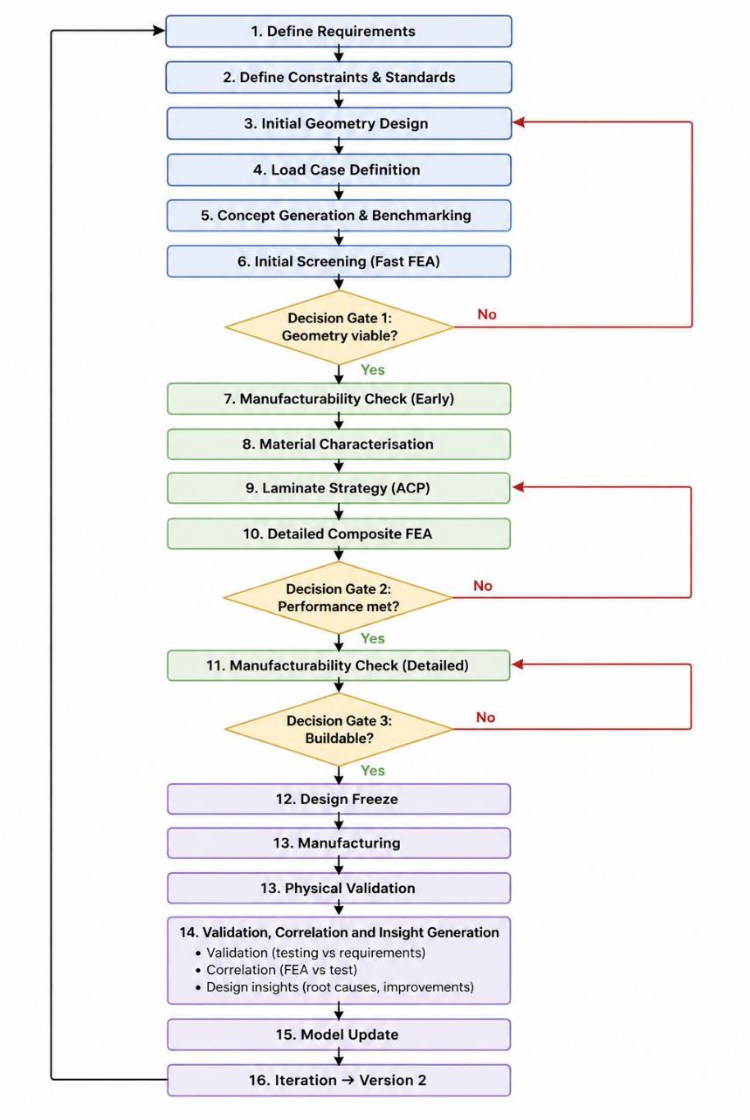

Figure 11 - Methodology Flow Chart

3.1. Requirements, constraints and benchmarking

By understanding the team’s aims, requirements were derived from regulations, benchmarking, and system integration constraints, then formalised into measurable targets. This ensured the wheel design addressed key areas including safety, legality, fitment, and performance. Safety considerations included structural strength, fatigue resistance, and environmental durability, while legality was governed by FSUK regulations and internal team standards. Fitment requirements ensured compatibility with the tyre, gearbox, and surrounding architecture, whilst performance focused on hitting mass and rotational inertia targets.

Legality

FSUK regulations define the allowable design space for wheel construction, interfaces, and safety features. The applicable rules and the corresponding design implications are listed below in table 3**.**

Table 3 - FSUK relevant rules to wheels (2025/26)

Rule ref	*Category*	*Requirement*
Wheel mounting & hardware - T2.4		
T2.4.2	Fastener	Standard wheel lug bolts and studs must be steel or titanium. Modified or custom designs require proof of good engineering practice. Studs must not be hollow.
T2.4.3	Fastener	Aluminium wheel nuts may be used only if hard anodized and in pristine condition.
T2.4.4	Wheel clearance	At all extremes of suspension and steering travel, the static radial clearance between the wheel rim and any non-rotating component must be ≥5mm. [2025 changelog addition]
T2.4.5	Composite	Extended or composite wheel studs are explicitly prohibited.
T2.4.6	Wheel spacer	Wheel spacers are permitted. Laminated or multiple spacers per wheel are not permitted.
T2.4.7	Wheel set	Wheels for dry and wet tyres may differ, but all four dry wheels must be identical and all four wet wheels must be identical.
T2.5.2	Tyre	Tyres on the same axle must have the same manufacturer, size and compound.
T10.1.1	Fastener	Critical fasteners include those in the suspension system. Wheel studs, hub bolts, and fasteners attaching the wheel carrier to the suspension are all critical fasteners.
T10.1.2	Fastener	All threaded critical fasteners must be at least 4mm metric grade 8.8, SAE Grade 5 or equivalent.
EV-specific - grounding & outboard motors [EV only]		
EV3.1.5	EV	The rotating part of the wheels does not need to be grounded.

Safety

As this is a safety-critical component, a minimum factor of safety of 2.0 was specified. The design was evaluated against representative load cases, discussed later in its own section, with additional allowances for impact and thermal effects. Pre-use verification was mandatory: CT/NDT inspection to confirm laminate quality, followed by physical load testing to demonstrate integrity under service-representative loading before any on-car driving. Figures 12 and 13 show some examples of load testing to ensure structural requirements are met.

Figure 12 - Physical test setup, testing radial loads

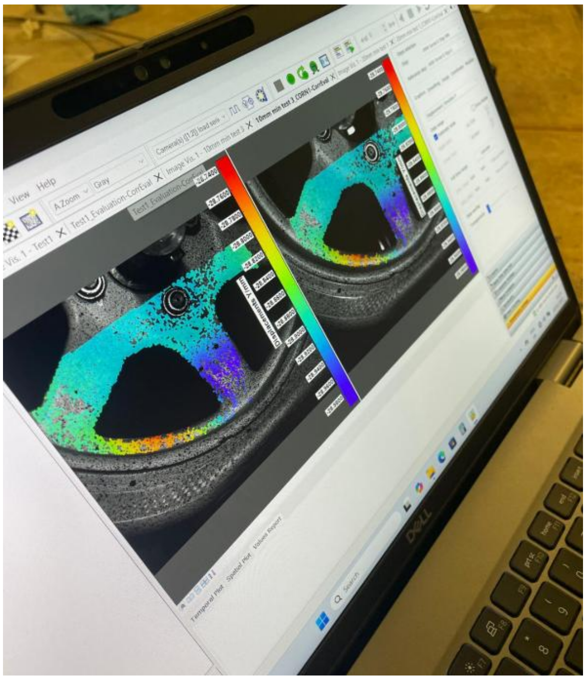

Figure 13 - deformation strain data from radial load test

Fitment

Fitment requirements ensured full compatibility with the tyre, hub/insert interface, and surrounding vehicle architecture. This included bead seat geometry checks against the ETRTO wheel rim standard, assembly access for fasteners, ample clearance to suspension/brake components, and control of runout to limit vibration and tyre wear. These checks were verified through CAD checks and physical inspection as shown in figures 14 and 15 below.

Figure 14 - Wheel fitment onto FS25 car

Figure 15 - Dimensional checks using a CMM

Performance

The primary performance metric was mass (and therefore inertia), informed by benchmarking against other commercially available wheels. Secondary targets included radial and lateral stiffness to preserve predictable handling and tyre contact behaviour.

3.2. Concept selection

The wheel architecture was selected by comparing four feasible concepts: (i) three-piece wheels (separate rim halves and centre), (ii) two-piece split rims, (iii) a single-piece composite barrel with a metallic centre, and (iv) a fully monolithic composite wheel with an integrated metallic insert at the hub interface. The comparison considered prototype cost, manufacturing complexity, structural efficiency, mass potential, and leak risk. Leakage is a common practical failure mode for FS wheels, hence was a highly weighted factor. The combination of performance and weights are represented below in table 4.

Table 4 - concept selection table splitting concepts into 4 categories and qualitatively ranking them

	concept i Three-piece split wheel	concept ii Two-piece split rim	concept iii Composite barrel, metallic centre	concept iv Monolithic composite with hub insert
COST & MANUFACTURABILITY				
Prototype cost	●●●○ low	●●●○ low	●●○○ moderate	●○○○ high
Manufacturing complexity	●●●○ low	●●●○ low	●●○○ moderate	●○○○ high
STRUCTURAL PERFORMANCE				
Structural efficiency	●○○○ poor	●○○○ poor	●●○○ fair	●●●● superior
Mass potential	●○○○ poor	●○○○ poor	●●○○ fair	●●●● superior
SEALING & SAFETY				
Leak risk	●○○○ high	●●○○ moderate	●●●● minimal	●●●● minimal
NOISE, VIBRATION & HARSHNESS				
NVH performance	●○○○ poor	●○○○ poor	●●○○ fair	●●●● superior

■ poor / high risk ■ fair / moderate ■ good / low ■ superior / minimal

Multi-part architectures (two- and three-piece) were rejected primarily due to their dependence on joint sealing and clamp preload stability. While these designs can simplify manufacturing and allow modular replacement, they introduce multiple seal paths and increase tolerance stack-up, which raises both leak risk and vibrations. They also add mass through flanges and fasteners, penalising the stiffness-to-weight objective.

The final decision was between a one-piece composite barrel with metallic centre and a fully monolithic composite wheel. Both offer good sealing as the barrel isn't split but the key difference was the balance between development resources and performance. A simple combined cost-mass KPI was used to support this, where both low cost and low mass are desirable. The KPI was defined as the product of unit cost and wheel mass (KPI = Cost × Mass), such that increases in either parameter worsen the score. Using benchmark estimates, the monolithic wheel achieved a KPI of 870 £·kg compared with 1,100 £·kg for the one-piece barrel with a metallic centre, representing an improvement of approximately 21%. Using table 5, the monolithic architecture was selected as the best combined performance-to-cost option.

Table 5 - Table showing architecture concept selection

CONCEPT	ARCHITECTURE	COST (£/WHEEL)	MASS (KG/WHEEL)	KPI = COST × MASS (£·KG)	RANK
Concept 4	● Monolithic composite rim	£600	1.45	870	1 1st
Concept 3	● Composite barrel + metallic centre	£500	2.20	1,100	2nd

Lower KPI = better combined performance. Concept 4 is ~21% better on the cost–mass metric.

This choice increased tooling and lay-up complexity beyond initial expectations, but it aligned with the project's broader aim of establishing a robust first-article for safety-critical components.

3.3. Initial geometry

With the overall concept fixed, the next stage was to define the initial wheel geometry in CAD. The external barrel geometry was governed primarily by the requirement to fit a 13 × 7J tyre, meaning the starting point was the ETRTO rim standard for this size. ETRTO is a standard that defines the key tyre seating features, including the bead seat diameter, rim width, flange profile, and associated tolerances required for safe tyre mounting and inflation.

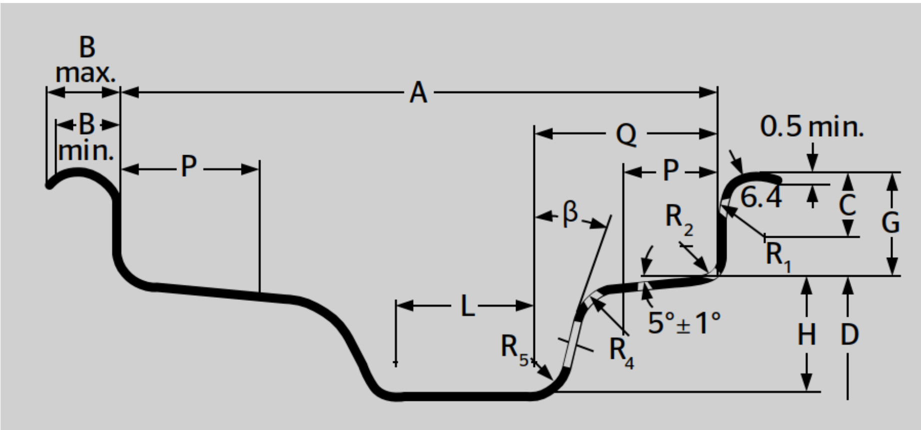

Rim Contour	Dimensions (mm)											
	A		B Min.	B Max. 1)	G ± 0,6	P Min.	H Min. 2)	L Min.	Q Max.	R_1 Min.	R_2 Max.	β Min.
3.00 B	76					13		16	28			10°
3.50 B	89					15		19	34			
4.00 B	101.5											
4.50 B	114.5		10	13	14.1		15			7.5	4.5	13°
5.00 B	127					19.5		22	45			
5.50 B	139.5											
6.00 B	152.5	± 1										
3 J	76					13		16	28			10°
3 ½ J	89					15		19	34			
4 J	101.5											
4 ½ J	114.5											
5 J	127											
5 ½ J	139.5											
6 J	152.5											
6 ½ J	165											
7 J	178											
7 ½ J	190.5											
8 J	203		11	15	17.3		17.3			9.5	6.5	20°
8 ½ J	216					19.5		22	45			
9 J	228.5											
9 ½ J	241.5											
10 J	254	± 1.5										
10 ½ J	266.5											
11 J	279.5											
11 ½ J	292											
12 J	305											
12 ½ J	317.5											
13 J	330											

Figure 16 - ETRTO standard design diagram – highlighted section for the applicable tyre size (13J)

Figure 16 shows ETRTO dimensions which formed the basis of the CAD model and were treated as non-negotiable design inputs. Some compromises were required to ensure the geometry remained manufacturable, including smooth transitions, and draft angle.

Once the ETRTO-driven barrel had been established, the internal wheel geometry was developed around the surrounding hardware. Clearance to the front suspension, and particularly the rear gearbox, defined the interface. These packaging constraints were imported into CAD, shown in figure 17 and 18, and used to establish a bounding volume for the wheel centre. Wheel offset became a major driver of this stage, using the teams CAD models of the wheel centre mounted to the front of the wheel hub and located on its main boss. This forced the centre section to sit significantly inboard relative to the barrel, creating the basis for the later spoke architecture.

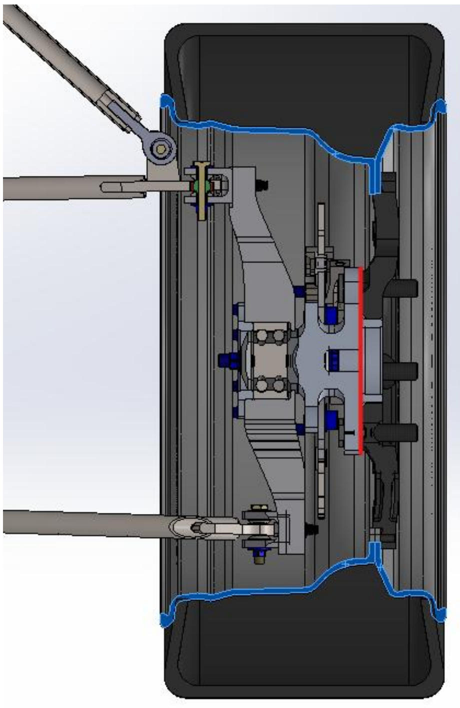

Figure 17 - front suspension with the blue contour of the wheel and red line showing the inward offset required to meet the wheel hub

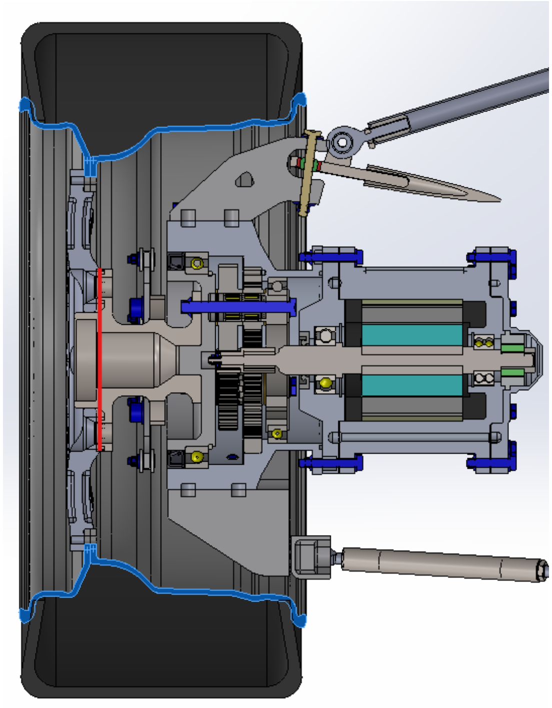

Figure 18 – rear suspension with the red line showing the inward offset required to meet the wheel hub

The wheel centre uses a co-cured metallic insert to provide a durable bolted hub interface, as direct fastening through the CFRP laminate is avoided because bolt bearing and clamp-up induced through-thickness stresses can initiate delamination [6]. The insert therefore provides a damage-tolerant load path and a stable contact surface for the hub joint, without the need to focus this section on the joint architecture.

Geometrically, the insert is constrained by the hub interface: the central bore and 4-bolt PCD are fixed to ensure correct mating. A simple disc form was selected to minimise machining complexity. The insert thickness was set by the fastening requirements: the nut uses a 60° conical seat, so sufficient thickness is required to maintain full cone engagement and prevent local shear-out under the governing load case. A technical drawing of the insert can be seen below in figure 19.

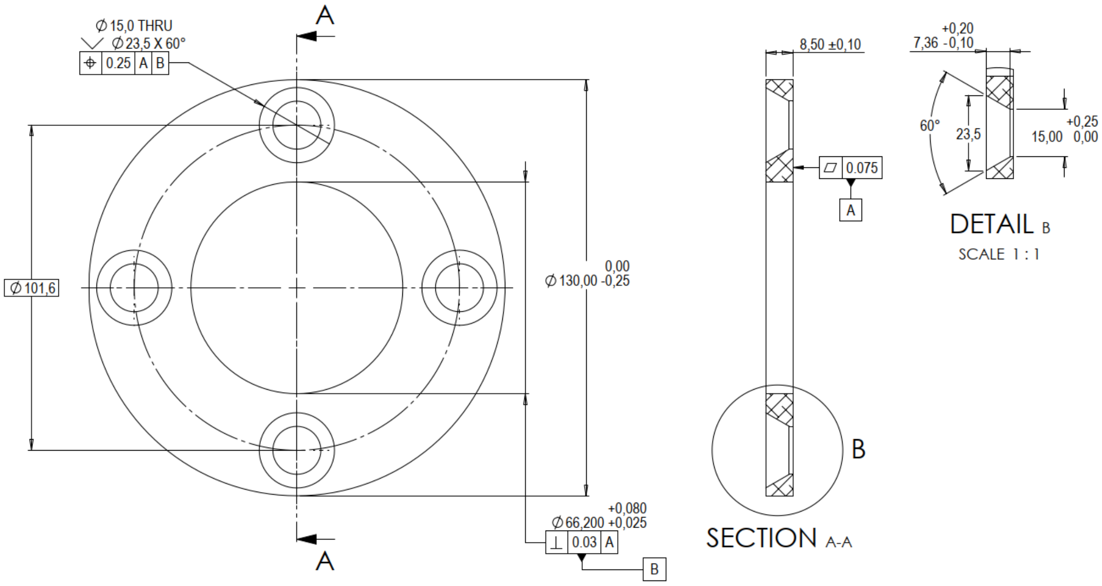

Figure 19 - final geometry of the metallic insert

Material selection for the insert prioritised high specific strength and straightforward procurement. Candidate alloys were screened using an Ashby chart which plots density vs. yield strength - shown in figure 20 - retaining only those above a target performance line and below a cost ceiling of £20/kg to avoid exotic options. This reduced the shortlist to aluminium and magnesium alloys. Given the team's limited experience with magnesium, Aluminium 7068 was selected as a lower-risk option offering adequate strength.

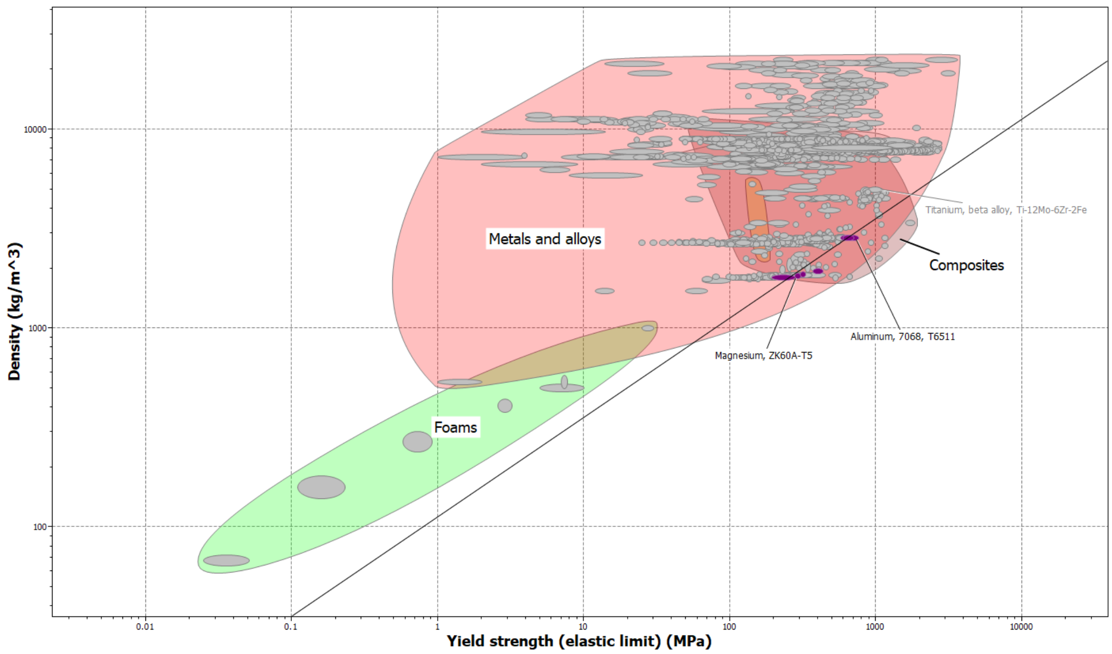

Figure 20 - Specific strength Ashby chart showing applicable aerospace materials for the insert. greyed materials fall out of the cost or strength requirement

3.4. Spoke Design

Following definition of the barrel and centre geometries, the spoke structure was developed as the primary load path between the hub interface and the wheel barrel. In particular, the wheel incorporated a negative offset of approximately 80mm, requiring the spokes to transition from the barrel drop-centre region inboard towards the gearbox mounting face, seen in figures 21-23.

Figure 21 - defined interface geometry isometric view

Figure 22 - defined interface geometry cross section

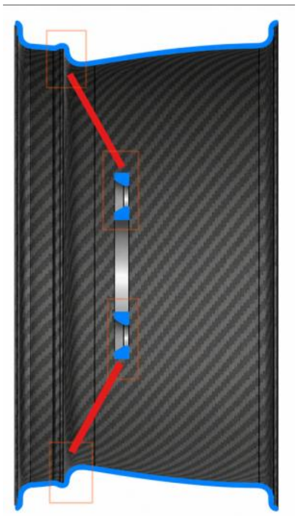

Figure 23 - defined interface geometry with highlighted spoke path

Simultaneously, adequate clearance was required for the brake calliper, suspension members, and adjacent drivetrain components.

The spoke count was chosen using a weighted trade study comparing five layouts - 4, 5, 6, 8, and 10 spokes - against mass, peak stress, and manufacturability. Each criterion was normalised to a 0–1 scale so they could be compared directly. Lower mass and lower peak stress were treated as favourable, while manufacturability was scored such that higher values indicated simpler manufacturing. The weighted total score for each option was then calculated from the normalised results shown in figure 24.

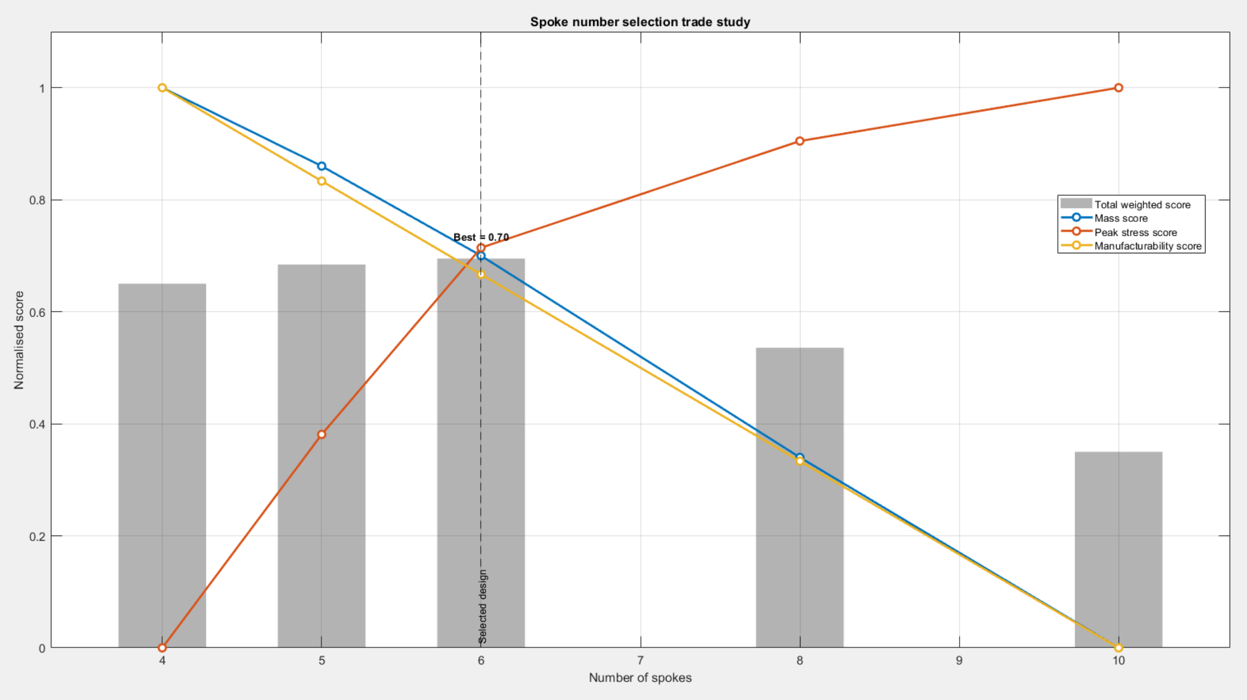

Figure 24 - Plot showing mass & manufacturability diminish with peak stresses plateau at 8 spokes - the bars represent total score

The outcomes were plotted with total weighted score shown as bars and the individual criterion scores shown as lines. Lower spoke counts gave low mass and reduced manufacturing effort but produced higher peak stress. Higher spoke counts reduced peak stress, but increased mass and manufacturing time. The six-spoke design achieved the highest total weighted score, with five spokes a close second, while eight and ten spokes showed diminishing returns due to mass and production penalties

Additionally, because the hub used a four-bolt pattern, a six-spoke layout was preferred for practical implementation. Using an even number of spokes simplified the design and test set-up by allowing symmetric features.

The initial spoke geometry therefore prioritised simplicity, packaging feasibility, manufacturability, and - to a lesser extent - aesthetics. A relatively wide, shallow spoke profile was adopted to provide a direct load path between the barrel and centre section while remaining compatible with the surrounding vehicle architecture.

At this stage, the emphasis was on developing a concept that satisfied the performance targets while remaining straightforward to manufacture. This established a practical foundation for subsequent refinement and optimisation using more advanced design and analysis methods.

Figure 25 - Final selected geometry

With the rough geometry selected, shown in figure 25, multiple design studies were carried out to identify initial stress raisers and assess how they could be reduced. These finite element studies were kept simple, using a metallic SolidWorks FE model, shown in figure 26, to evaluate the effect of spoke root fillet radius under axial and radial loading. A parametric sweep was run from 2 to 20 mm, and peak stress and mass were extracted for each case to highlight where further increases in radius provided diminishing returns. Based on this screening, a 12 mm fillet was selected as the best compromise, giving the lowest peak stress while avoiding unnecessary mass increase.

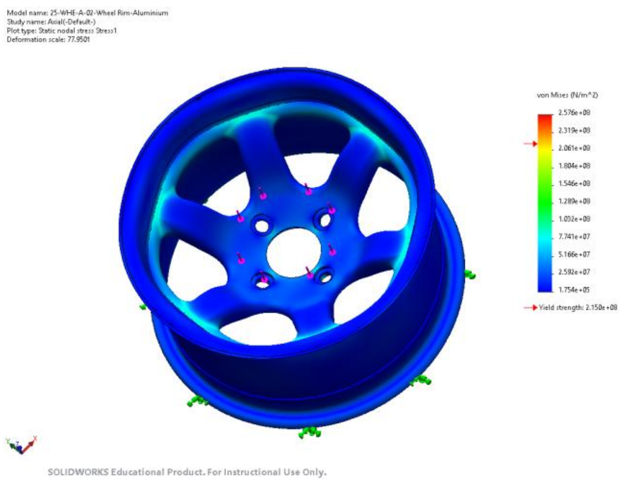

Figure 26 - Initial FE model in solidworks showing stess raisers around the spoke-barell interface

With the geometry decided, two spoke cross sectional concepts were subsequently investigated: an open C section geometry without a foam core, and a closed box section incorporating a lightweight foam core. The objective of this comparison was to investigate whether laminate skin separation could significantly improve stiffness without requiring additional composite material.

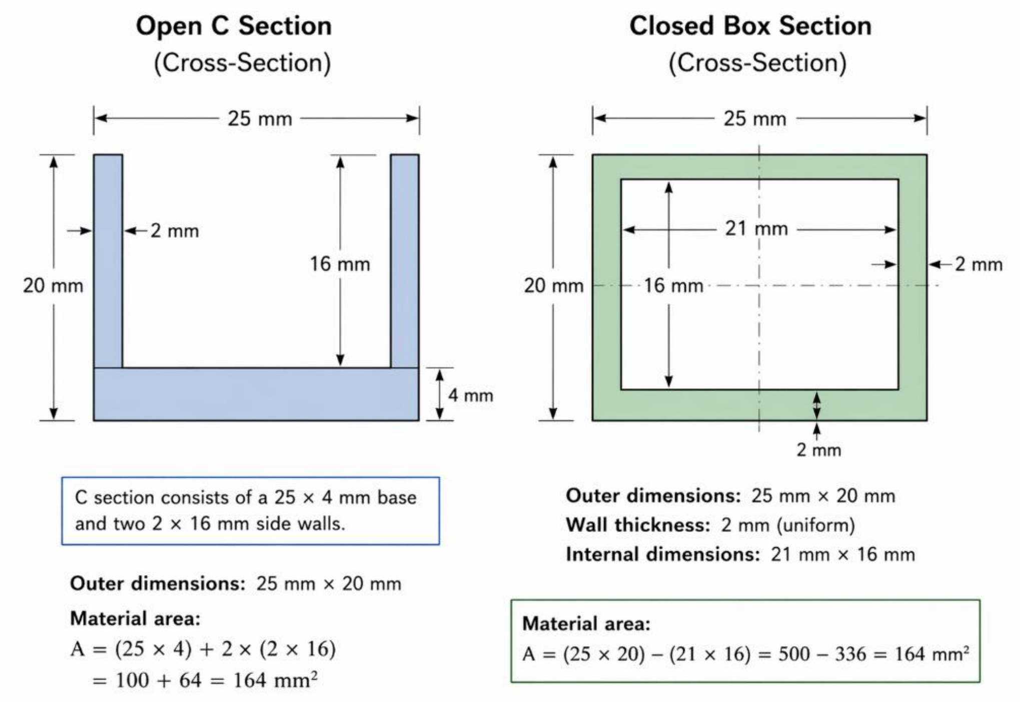

Figure 27 - Concept A & B cross-section geometries

To compare the structural behaviour of both concepts, simplified first principle calculations were carried out using representative cross-sectional dimensions. The open C section and closed box section were both defined using identical outer dimensions and equivalent material area, allowing the effect of geometry alone to be isolated. Using standard second moment of area calculations,

$$I_x = \frac{bh^3 - b_i h_i^3}{12}$$

$$I_{x,\,closed} = \frac{25(20)^3 - 21(16)^3}{12} \approx 9500 \text{ mm}^4$$

The C section consisted of a 25 × 4 mm base and two 2 × 16 mm side walls. The centroid location was calculated as:

$$\bar{y} = \frac{100(2) + 32(12) + 32(12)}{164} = 5.9 \text{ mm}$$

Applying the parallel axis theorem to each element gives:

$$I_{x,\,C} \approx 5400 \text{ mm}^4$$

This corresponds to an increase in geometric bending stiffness of:

$$\frac{9500 - 5400}{5400} \approx 76\%$$

This increase in stiffness is primarily driven by redistributing material away from the neutral axis, which raises the section's bending resistance with minimal mass increase. The results suggest that structural response is governed more by laminate separation, however, the hand calculations neglect key effects such as 3-dimensional geometry, material anisotropy, and core behaviour - so the concept was progressed to finite element analysis for further investigation.

3.5. Load case definition

The load case definition stage was used to determine the forces and moments acting on the wheel during representative Formula Student operating conditions. These values translated the project requirements into numerical design inputs for finite element analysis and physical validation. During operation, the wheel experiences longitudinal loading during acceleration and braking – alongside torque transfer through the hub interface - lateral loading during cornering and vertical loading from bump and kerb strikes. These loads occur at different directions, shown in figure 28, but also magnitudes and combinations throughout vehicle operation, both peak strength and fatigue load cases were required to be understood for full analysis.

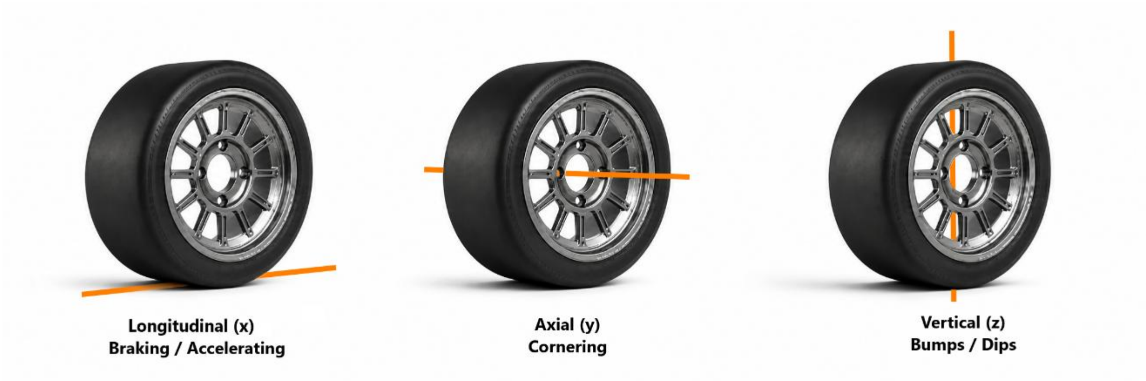

Figure 28 - Axis and load directions

These cases were developed using three primary sources: theoretical vehicle dynamics calculations, vehicle simulation outputs, and physical track testing. Initial theoretical calculations were based on an existing team load case spreadsheet developed by Alumni, Daniel Serenti. Outlined using methods derived by Seward and Milliken. This spreadsheet estimated the forces acting at each wheel during representative vehicle manoeuvres including acceleration, braking, cornering, and a 3g vertical bump load. These calculations, summarised in table 6, formed the initial basis for the structural design requirements of the wheel.

Table 6 - Load cases from Sorrenti

Load Case	***Magnitude***	***Direction***
Braking	1633 N	Longitudinally
Cornering	1940 N	Axially

Bump (Vertical)	2060 N	Vertically
Torque	420 / Nm	Rotationally (clockwise)

Figure 30 shows the teams in-house lap time simulation model which was used to simulate the FSUK circuit. This provided representative vehicle acceleration behaviour throughout a full lap and allowed comparison between the theoretical loads and simulated accelerations allowing comparison. The shown accelerations are seen in figure 30 and by multiplying by these by the product of vehicle mass and gravity we can approximate loads of 2402N in X and 1994N in Y. The simulation did not consider potholes or bumps, hence generating incomparable values.

Force = Acceleration x (vehicle mass + driver) x 65% / 2

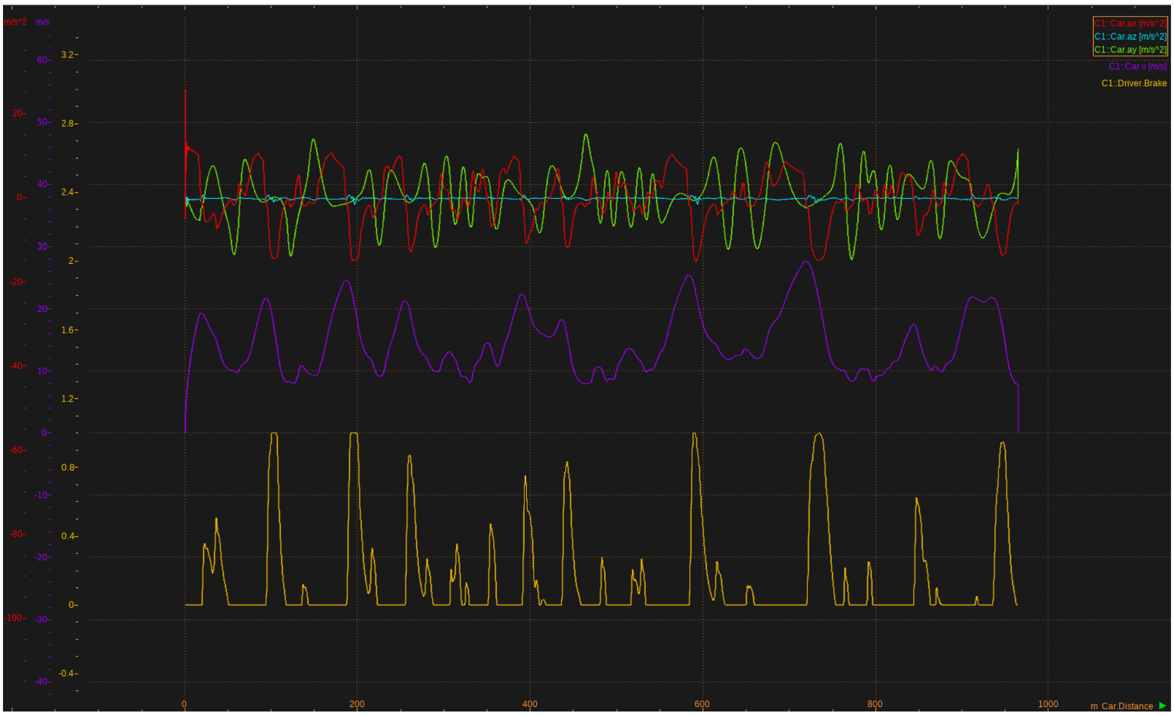

Figure 29 – FSUK Endurance (final race) lap time simulations showing service loads

To validate the theoretical and simulated methods, physical track testing was carried out using the FS25 vehicle during post season testing, which shared architecture to the intended FS26 design. Testing included acceleration, cornering, and race running under representative operating conditions. Vehicle dynamics data was collected using a 9-axis IMU incorporating accelerometer, gyroscope, and magnetometer sensing. The recorded acceleration data was then converted into representative wheel loads using vehicle mass and load transfer relationships.

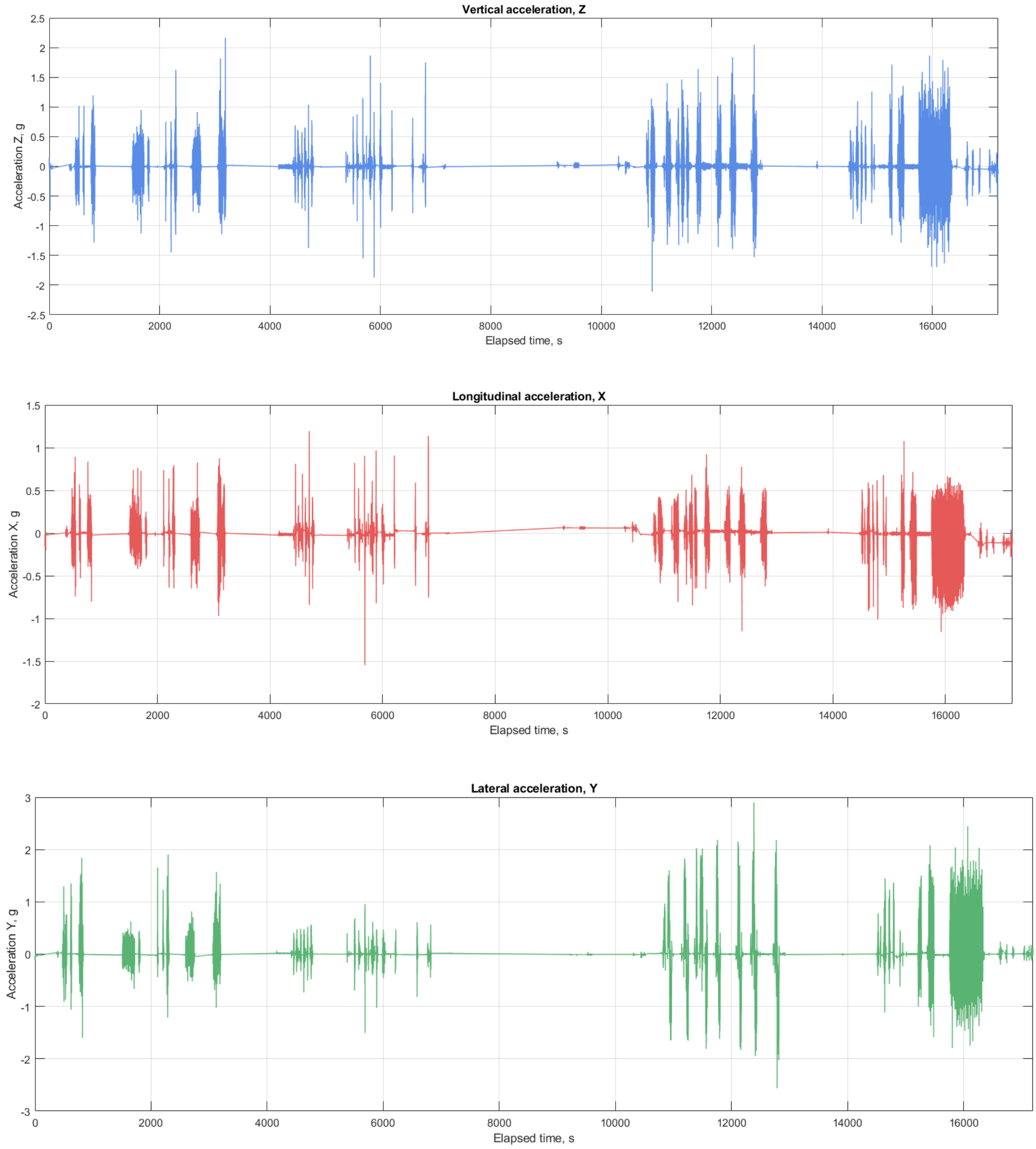

Figure 30 – Plotted acceleration loads data from on-campus track testing 13-04-26

As before with simulations, the acceleration values are converted into wheel loads and correlation between these three approaches provided confidence that the final design loads were both realistic and suitably conservative for structural analysis.

Table 7 - Correlation table showing all loads for each method

Loads	*Calculations*	*Simulation Data*	*Testing Data*
Longitudinal (X) / N	1633	2402	1999
Axial (Y) / N	1940	1994	2209
Vertical (Z) / N	2060	-	2314
Torque / Nm	420	-	404

Table 7 compares the three load evaluation methods. Theoretical calculations provide a fundamental baseline but do not account for transient loads or real-world variability. Simulation captures more representative vehicle behaviour but remains sensitive to modelling assumptions and operating conditions. Physical track testing provides the most representative estimate of service loads, despite variation from driver behaviour and track conditions. Consequently, the measured test loads were adopted as the design basis and multiplied by a safety factor of 2 to ensure sufficient design margin while allowing future optimisation as additional validation data becomes available.

3.6. Composite Process

Manufacturing and tooling were considered from the outset because wheel geometry and manufacturability were tightly coupled: the design constrains feasible processes, while process and tooling limits constrain achievable features and quality. The geometry was therefore iterated alongside process and tool selection to ensure compatibility with lay-up, curing, and mould construction. Manufacture was planned for low-volume prototyping, balancing structural performance against tooling complexity, facility capability, material availability, and defect risk.

Composite process

Composite manufacturing methods were selected based on three criteria: minimising defect risk for a rotating safety critical component, compatibility with available manufacturing facilities, and suitability for future production scalability. Figure 32 summarises the manufacturing workflow.

Resin infusion was considered for its low tooling cost, but the wheel geometry (spoke transitions and integrated features) makes resin flow highly sensitive to lay-up compaction, flow-media placement, vacuum integrity and venting strategy. This introduces multiple interacting variables and increases the likelihood of non-uniform wet-out, local dry regions and fibre disturbance, reducing confidence in repeatable quality. RTM offers excellent control and production repeatability, but it requires matched tooling and dedicated injection equipment that were beyond the project’s practical capability and disproportionate for a prototype programme. Prepreg was therefore selected: controlled resin content and fibre architecture reduce reliance on in-plane resin flow, improving consistency in complex regions, while remaining compatible with low-volume prototyping and scalable process control for future iterations.

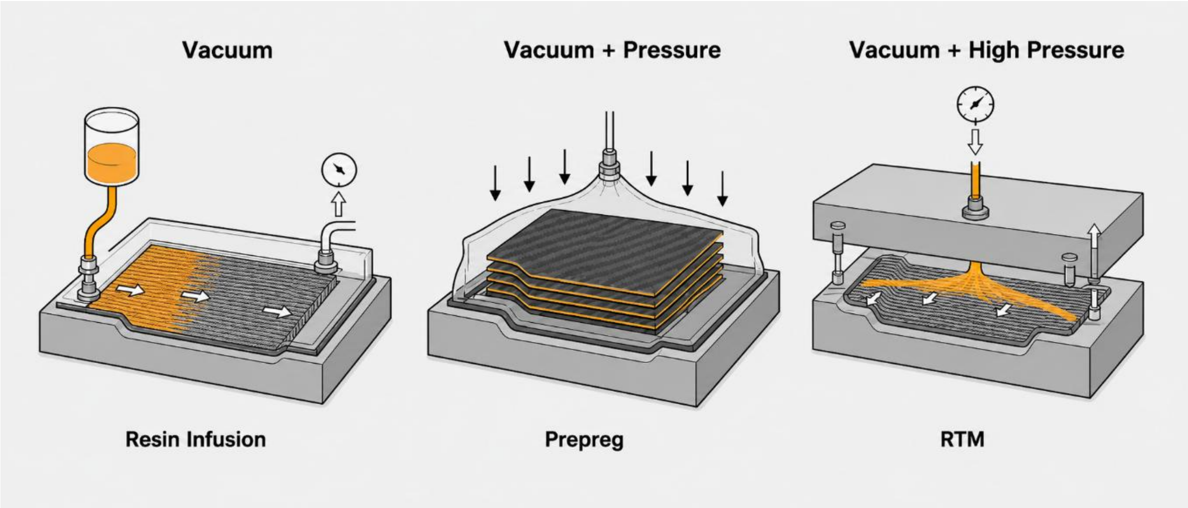

Figure 31 - Diagrams showing the overall concept of each manufacturing process with the resin represented as orange and carbon as black with grey representing the mould surface

Tooling Strategy

Carbon fibre is made from fabric-like sheets that are laid into a rigid mould shaped as the reverse of the final part, building up multiple layers to create the component. Because the lay-up is cured in an autoclave, the mould must be strong enough to withstand around 6 bar pressure and remain dimensionally stable at elevated temperature - meaning it should not soften or warp and should have a low coefficient of thermal expansion (CTE) so it doesn't change shape as it heats.

The tooling strategy was defined by the constraints of low-volume prototype manufacture. Tooling for automotive components is typically metallic (aluminium or steel), due to its dimensional stability, durability over hundreds of parts, and ability to be machined to tight tolerances. However, for a 13-inch wheel mould, the estimated upfront cost was £400–£600, driven by material and machining requirements. Given the high likelihood of design iteration during prototype development, and the resulting need to repeat these costs, an alternative, cheaper, tooling approach was required.

Epoxy tooling board, shown in figure 33, is low cost alternative developed for this exact reason. Epoxy is lightweight, cheaper and has excellent thermal stability. However, a key limitation of epoxy toolboards is its lower temperature resistance which makes it prone to crack. This means that the wheel will require extra processing with an initial cure to 130C, then removed, then post cured to 180C in an oven. Furthermore, the likelihood of getting more than 2 components without damage to the mould is minimal.

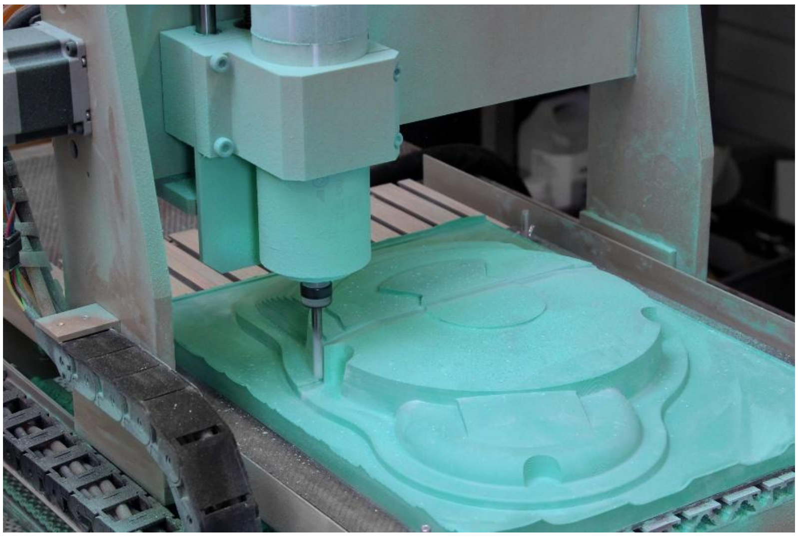

Figure 32 - CNC machining of epoxy toolboard

Carbon tooling was also considered but fit better for later development once the design was validated. It would improve durability, handling, and thermal compatibility with the part, notably through matching the CTE of the carbon part to the carbon tool. However, producing a carbon tool would introduce an additional manufacturing cycle before any wheels could be made. For the first prototype stage, direct tooling provided the fastest and most cost-effective route to a representative functional component.

Cure Cycle

Autoclave manufacture of the wheel assembly required balancing process simplicity against yield and inspect ability. One option was to cure the composite structure first and bond the metallic insert afterwards, which would improve inspection access and potentially increase yield. However, it would add surface preparation, alignment/fixturing, and a secondary bonding operation, introducing extra time and process variability.

A more integrated route was therefore pursued: the lower section could be laminated first, then combined with the upper section to loop and consolidate the laminate across the split region. The metallic insert and foam core were co-cured to produce a single moulded component and minimise the number of cure cycles. With limited autoclave availability and long cure occupancy, reducing the number of cures was a key manufacturing constraint.

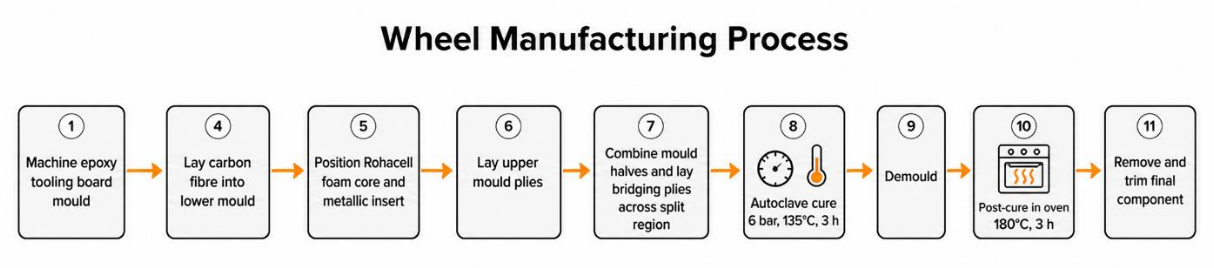

Figure 33 - Selected manufacturing process

Overall, the selected route, illustrated in figure 34, prioritised rapid prototyping over production efficiency. A direct epoxy tooling board mould provided a low-cost, fast-turnaround option for an iterative, complex geometry, while prepreg carbon fibre supported consistent lay-up quality within the available facilities. The wheel was produced as a single integrated assembly using a one-shot autoclave cure followed by an oven post-cure to meet material performance requirements. While not the lowest-risk approach, it made advantage of materials and processes developed for prototype applications where the main constraints was budget, autoclave access, complex geometry and the need for a representative part for validation.

3.7. Composite Finite Element

Once the manufacturing method, material system, and geometry are fixed, final structural analysis can be completed to reduce the risk of costly, late-stage failures. The purpose of this analysis is to predict load paths and identify likely failure locations and margins before manufacture, allowing issues to be designed out while changes are still cheap. For composite structures, this step is particularly important because seemingly minor changes in ply orientation or reinforcement can significantly alter stiffness and strength without any visible change in geometry. Simulations provide the primary means of verifying that the structure will meet its requirements.

FEA was performed in ANSYS ACP to predict the composite wheel’s structural response under load. The laminate was defined ply-by-ply using fibre orientations from rosette mapping, measured ply thicknesses, and material properties from coupon testing, enabling a representative lay-up model of load transfer through the spokes, hub, and barrel. Initial testing is demonstrated in figures 35-38.

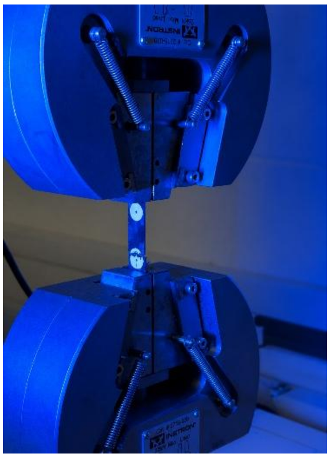

Figure 34 - composite dog bone sample with visible crack post tensile testing

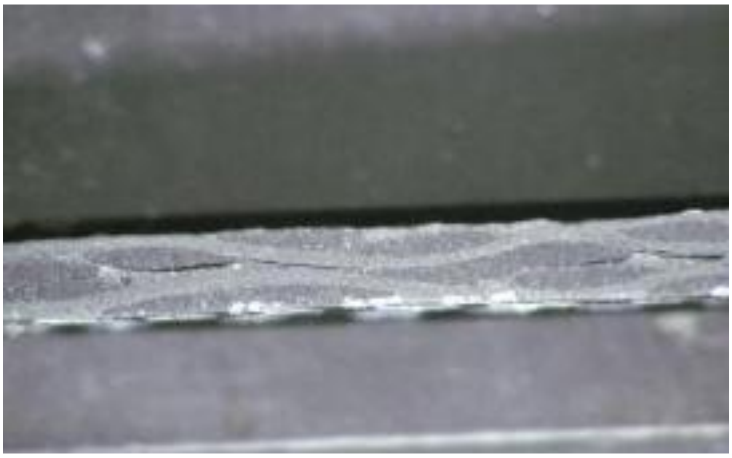

Figure 35 – Sample 3, 2mm thick, 10mm wide & 150mm long. cross section of sample removed mid test, showing delamination and cracks appearing in the structure

Property	*Units*	*Data Sheet*
Compressive strength	MPa	483
Tensile strength	MPa	470
Tensile modulus	GPa	55.1
Flexural strength	MPa	777
Flexural modulus	GPa	46.7
Interlaminar shear strength	MPa	64.7

Figure 36 - material properties used for FE simulations

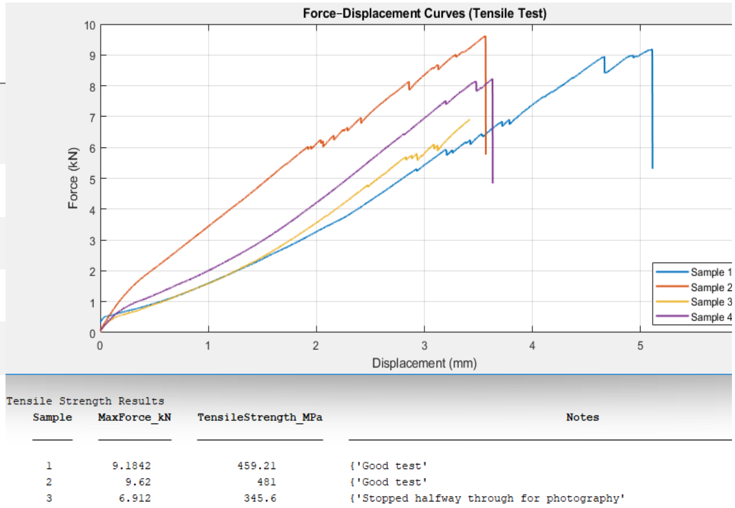

Tensile Strength Results

Sample	MaxForce_kN	TensileStrength_MPa	Notes
1	9.1842	459.21	{'Good test'
2	9.62	481	{'Good test'
3	6.912	345.6	{'Stopped halfway through for photography'

Figure 37 - Tensile testing data plot of carbon fibre sample

Using ANSYS ACP, the wheel model can be imported and loaded to replicate in-service conditions. The FEA is used to (i) define the required ply count and fibre orientations to prevent failure across critical load cases, (ii) optimise the lay-up by adjusting orientations and adding local reinforcements to reduce mass while maintaining stiffness and strength, and (iii) predict structural performance before manufacture to inform the iterative design process.

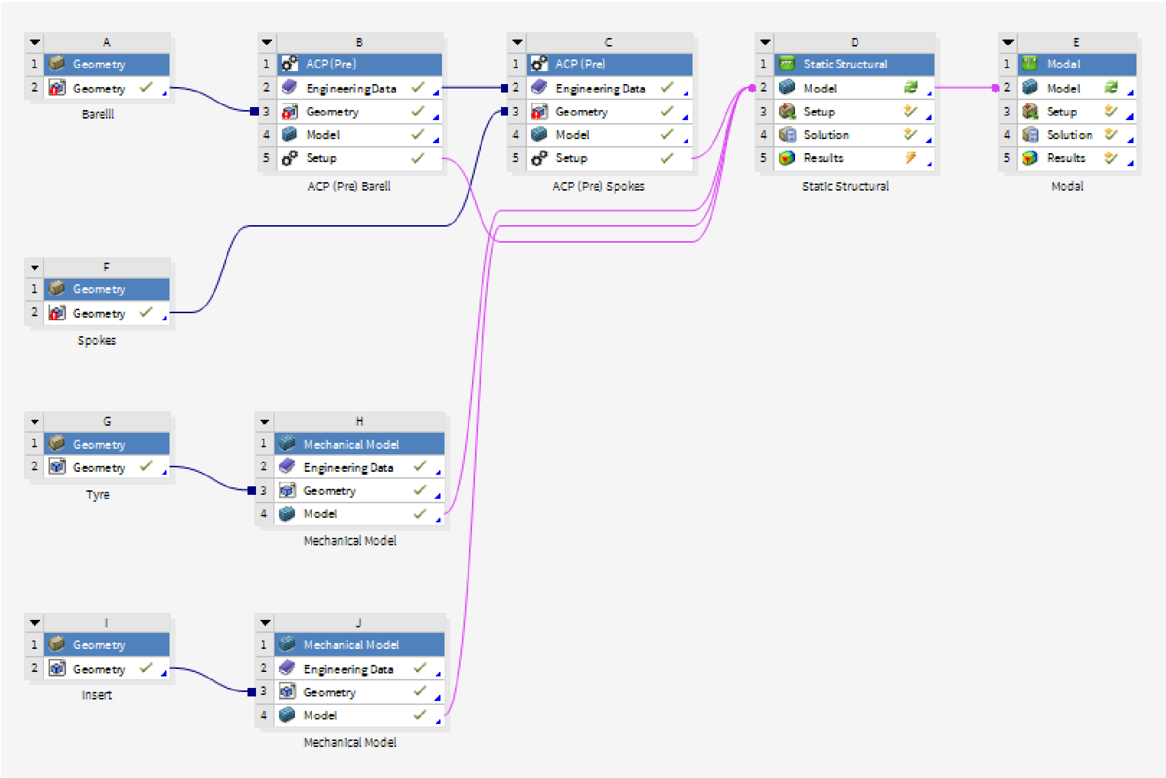

Figure 38 - ANSYS ACP workflow, importing bodies in, solid bodies meshed in a mechanical and surfaces meshed in ACP (pre) - then combined in a top level static structural and connections verified in a modal analysis

The finite element analysis workflow is demonstrated in figure 39 and throughout 40-51. ANSYS ACP models the composite as a layered shell built from the wheel's surface geometry, with a 2D surface mesh used to define ply stacking, fibre orientations, and through-thickness integration at each element. Metallic components are treated separately and meshed using a conventional 3D solid mesh, allowing the different material behaviours and thickness definitions to be handled appropriately. Where required, mesh refinement was applied in high stress-gradient regions (e.g., spoke–hub transitions and bead-seat features) to improve resolution of local stress and load transfer without an excessive overall element count.

Figure 39 - Initial total assembly mesh of 30k elements

ACP defines composite materials by combining constituent fibre and matrix properties into an equivalent lamina model. The user then assigns rosettes (and other orientation controls) to map local fibre directions onto the surface mesh and specifies the ply stack sequence, which together define the laminate thickness and fibre orientations across the geometry.

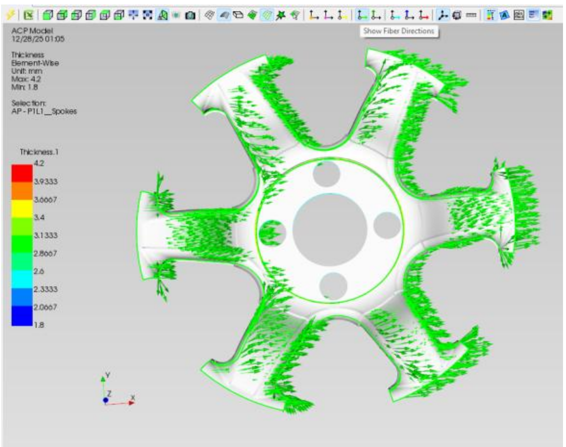

Figure 40 - ACP applying fibres to the model, showing directional fibres

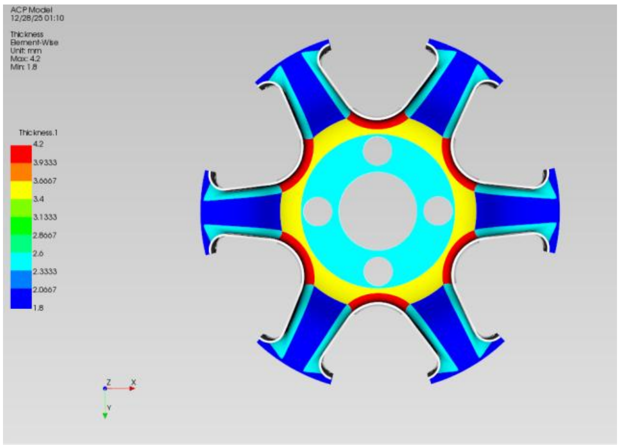

Figure 41 - ACP applying multiple layers to produce thickness

Once the composite lay-up model was defined, it was coupled to the metallic insert within the Static Structural solver using body-to-body connections to enforce the correct mechanical interaction between parts. Since the insert was assumed to be fully bonded to the composite, a rigid (fixed) bonded connection was used at the interface, constraining relative motion by pairing the displacements of the two bodies across the shared boundary.

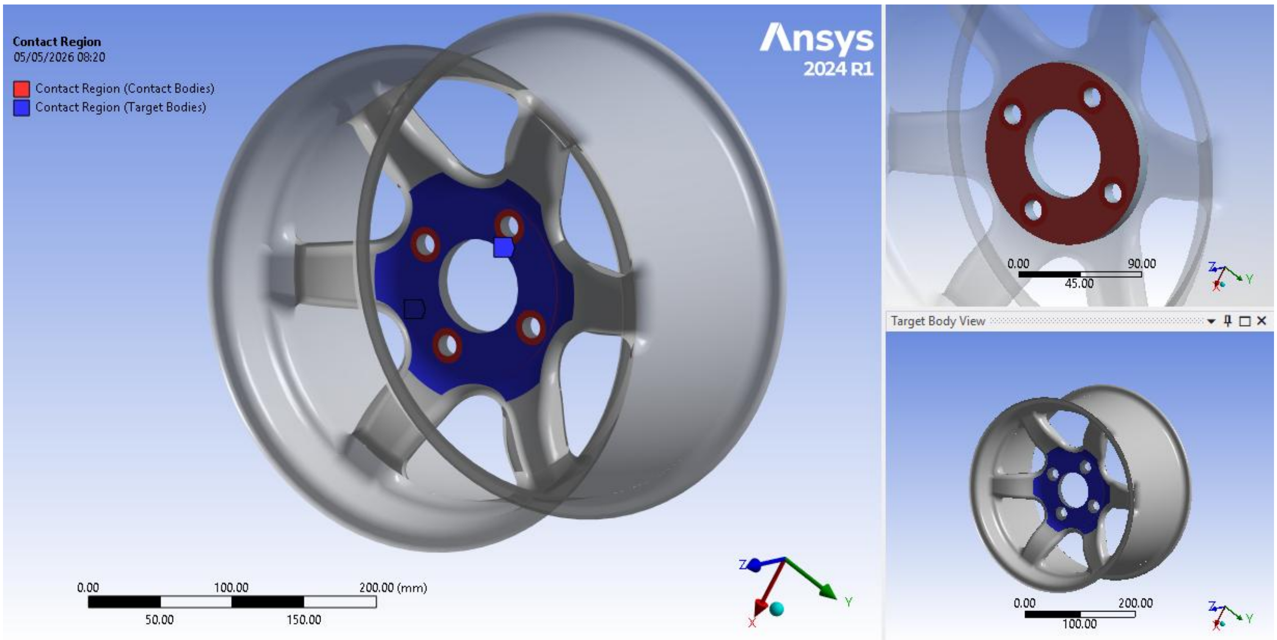

Figure 42 - Throughout the project connections were modified depending on insert design, mesh strategy and wheel architecture - but primarily the insert was bonded (assumed a rigid connection) to the wheel centre

Before running the static load cases, a modal analysis was performed as a sanity check on the assembly constraints and interfaces. Exciting the coupled system allows the composite and insert to vibrate as a single structure; any unintended relative motion or disconnected behaviour at the interface would indicate an issue with the defined connections. The modal response showed the model behaving as expected, with the composite and insert deforming in tandem and no relative motion at the bonded interface, indicating the connection definition was functioning correctly.

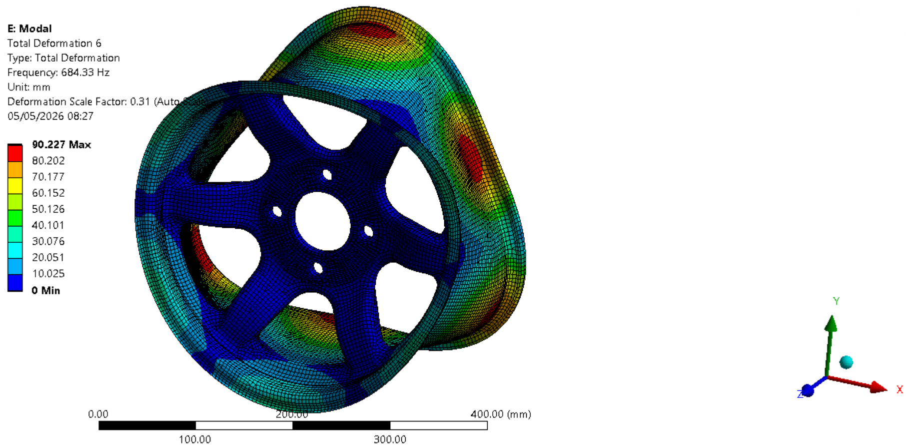

Figure 43 - Mode 1, 310.8Hz

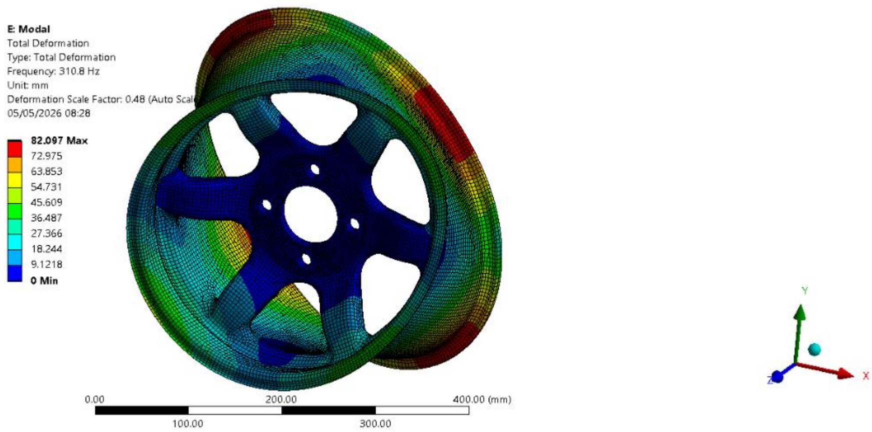

Figure 44 - Mode 6, 684.33Hz

After confirming the interface connections behaved correctly, boundary conditions were applied for an axial stiffness assessment: a 10kN load was applied through the wheel centre, with the lower rim lip constrained to represent the test fixture.

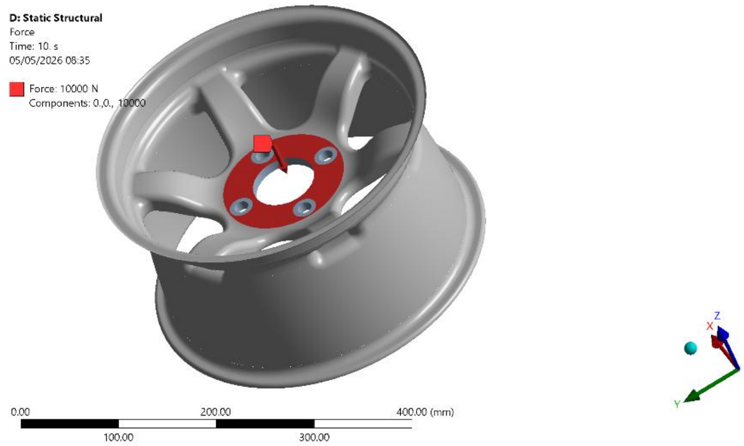

Figure 45 - Wheel centre loaded at 10kN

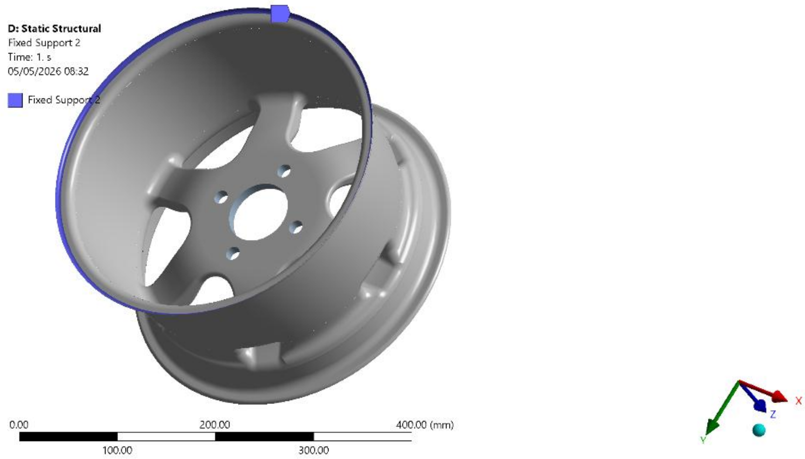

Figure 46 - Wheel inboard lip fixed

With the load case defined, a mesh convergence study was performed to confirm the results were not driven by element size. FEA approximates a continuous structure with discrete elements - if the mesh is too coarse, stress gradients near fillets, interfaces, and load application points are under-resolved, which can distort peak stress. The mesh is therefore refined until key outputs change negligibly, indicating a mesh-independent solution. Here, increasing the mesh from ~40k to ~65k elements produced minimal change in stress, indicating convergence.

Table 8 - Convergence plot and raw data from FEA study

Size (mm)	*Elements*	*ISF Max*	*Max Defl.*	*Max Strain*	*Max Stress (MPa)*	*Δ ISF*	*Δ Defl.*	*Δ Strain*	*Δ Stress*
3.5	37402	0.589	0.713	0.00664	385.3	6.89%	0.58%	5.53%	7.56%
3.0	39880	0.630	0.717	0.00700	414.5	-1.01%	0.40%	5.29%	6.57%
2.5	44604	0.624	0.714	0.00737	441.7	9.51%	0.49%	1.93%	-1.57%
2.25	48063	0.683	0.717	0.00723	434.8	13.22%	0.36%	3.86%	4.54%
2.0	52115	0.773	0.720	0.00751	454.5	-0.32%	0.72%	2.32%	-1.69%
1.5	65889	0.771	0.715	0.00734	446.8	—	—	—	—

With the solution converged, the simulation outputs were assessed against the two key success criteria: a global axial displacement below 1mm and composite failure indices remaining below unity. The predicted deflection met the target, and the inverse reserve factor/failure criteria indicated no onset of ply failure under the applied load. For interpretation, von Mises stress was treated as a secondary visualisation only, since the laminate is anisotropic and carries load differently along and across fibre directions. Failure assessment therefore relied on composite-specific criteria, which resolve fibre and matrix-dominated modes as a function of local ply orientation.

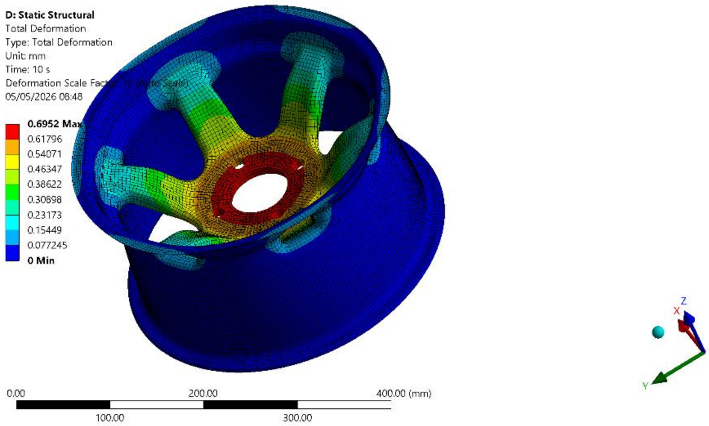

Figure 47 - Total deformation with 10kN applied

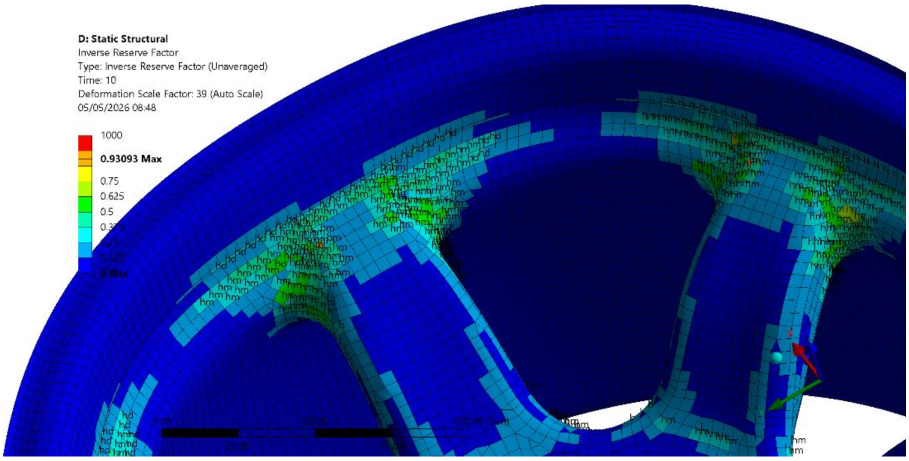

Figure 48 - Inverse safety factor, values above 1 show failure

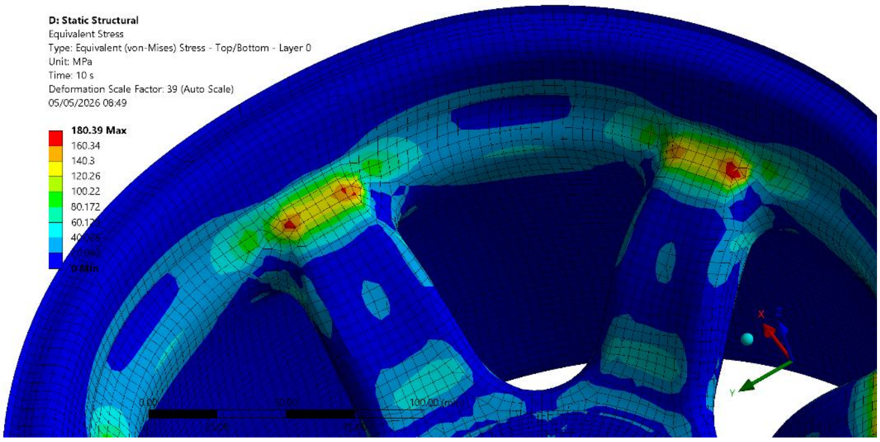

Figure 49 - Von Mises Stress, showing stress raisers throughout the structure

Under the applied axial load case, the predicted global deformation was within the target stiffness envelope (peak displacement ≈0.70mm) and the laminate did not indicate failure, with Tsai–Wu and Puck indices. Stress and failure index concentrations were consistently highest at the barrel–spoke transition, suggesting this region governs the load path and would benefit from local reinforcement or geometric smoothing in subsequent iterations.

Core vs no core

To simulate how the effects of adding a foam core would affect the stiffness response of the wheel. Both an axial and radial load cases were applied up to 10kN to provide a consistent basis for comparison across the aluminium baseline, variation 1 (no core) design, and variation 2 (foam core) configuration. Two test setups were simulated:

- An axial test simulated a simplified cornering load. Applying a load onto the central hub whilst fixing a flange wall.
- The radial test simulated a more realistic operating condition, with the tyre mounted at its rolling diameter and load applied through the central hub. This indicates radial stiffness is dominated by rim and tyre compliance rather than spoke geometry.

The resulting deformation was measured as displacement between the hub and bead region. Results showed minimal variation between designs, with aluminium at 0.44mm, variation-1 at 0.42mm, and variation-2 at 0.36mm. As expected, the inclusion of the foam core did not significantly influence radial stiffness, indicating that this load case is dominated by overall wheel geometry and tyre interaction rather than spoke section efficiency. Due to these relatively small differences, radial performance was not prioritised for further physical validation.

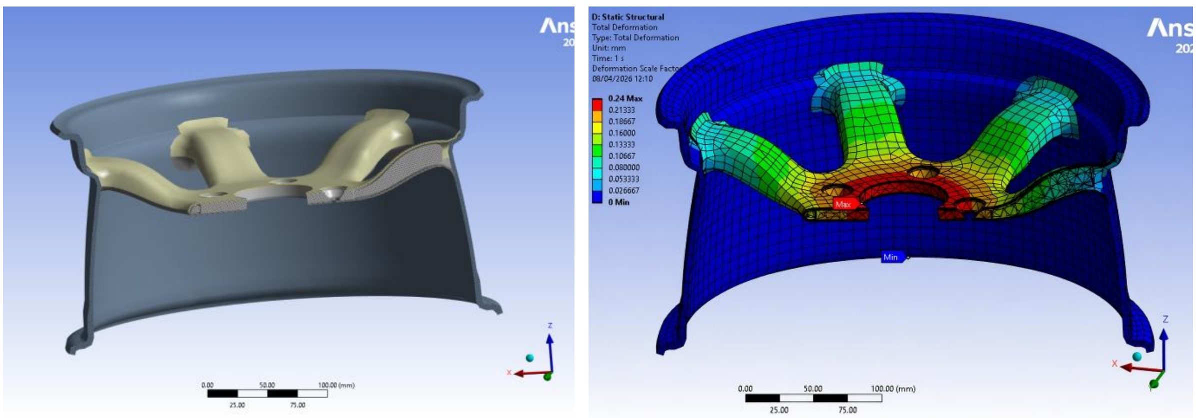

Figure 50 - FE model simulating an axial test to V2 (foam core) applying 10kN vertical load with 0.24mm of vertical deflection

Table 9 - FEA results from 10kN axial load

Design	*Radial Sim – Deflection @10 kN (mm)*	*Axial Sim - Deflection @ 10 kN (mm)*	*Change vs C-Section*
Aluminium	0.44	0.36	
V1 (no core)	0.42	0.23	—
V2 (foam core)	0.36	0.14	−42% axial deflection ≈ +71% stiffness

Table 8 highlights the key structural benefit of the composite designs. With the wheel supported at the flange and loaded centrally to 10kN without a tyre, significant reductions in deflection were observed. Aluminium exhibited 0.36mm deflection, compared to 0.24mm for V1 and 0.14mm for the V2 foam core design. This corresponds to approximately a 42% reduction in deflection between V1 and V2, translating to a stiffness increase of around 71%. This aligns closely with theoretical predictions of approximately 76% improvement based on second moment of area considerations for closed section geometries. The small discrepancy can be attributed to modelling assumptions, material variability, and manufacturing imperfections not fully captured in the simulation, but overall, the results validate the expected structural advantage of the foam core concept.

3.8. Production and Tooling Design

Once the wheel geometry and laminate thicknesses were finalised, the work transitioned from structural definition to production preparation, with emphasis on designing a manufacturable mould, developing cuttable ply templates, and compiling clear work instructions to ensure repeatability.

A split line was first defined to enable demoulding and to accommodate the wheel's spoke and hub features without undercuts. The split location was selected to maintain access for lay-up and core/insert placement and allow adequate draft angles on both upper and lower moulds.

Mould Design and Manufacture

The mould was designed as an internally tooled. Tool surfaces were derived directly from the wheel CAD by extracting the internal wheel surfaces, generating the negative mould geometry. The mould halves were designed to be bonded from multiple epoxy-board sections, CNC machined to final form, and then prepared for lamination. Alignment and repeatability were controlled through dowels and dedicated tooling features, including mating faces, bolt locations, and defined datum surfaces to constrain assembly. Additional features were incorporated to locate the metallic insert and to control core positioning during lay-up. Figures 53-56 show the initial tooling design.

Figure 51 - Lower mould CAD

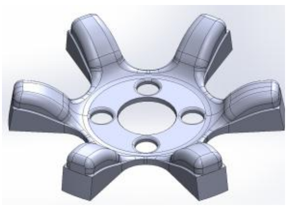

Figure 52 - Interchangeable centre for C-channel (no foam) variant

Figure 53 - Interchangeable centre for solid (foam) variant

Figure 54 - Upper mould CAD

A 1.0052 scale factor was applied to the tooling geometry to compensate for cure-temperature expansion and cure-related dimensional change in the BE978 epoxy tooling board. The mould is 380mm in diameter, the cure temperature is 135 °C, and CTE = 45×10^{-6} °C^{-1}, giving a predicted expansion of 0.52%, helping the cured component meet the intended dimensional tolerances.

The change in tool diameter was estimated using $\Delta D = \alpha D \Delta T$:

$$\Delta D = (45 \times 10^{-6}\ °C^{-1})(380mm)(135 - 20)\ °C = 1.97mm. \text{ or } 0.52\%$$

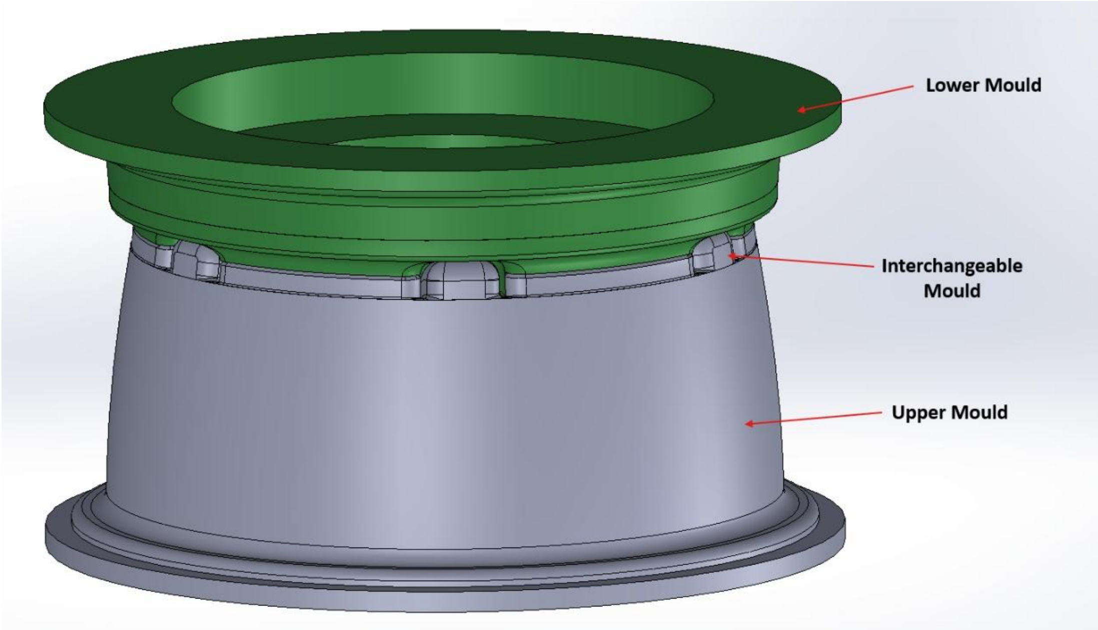

Figure 55 - Final mould CAD

Ply definition, flattening and nesting

Following mould definition, ply templates were developed for each region of the wheel. Due to the limited drapeability of woven and unidirectional prepreg, the laminate could not be applied as a single continuous 2D sheet over the full 3D geometry without introducing wrinkles, bridging, or uncontrolled fibre distortion. Instead, the wheel was segmented into manufacturable regions and the ply shapes were created to suit local curvature and fibre-direction requirements.

This process began by defining projected split lines in CAD to partition the wheel into logical lay-up zones. Surface patches were then created for each zone, and these were transferred into a dedicated drape and ply-development environment (Anaglyph). Within this software, a material definition was applied and the simulated drape behaviour was assessed to estimate fibre rotation, shear and wrinkling tendency. Where fibre re-orientation was excessive, regions were subdivided further into smaller ply segments to maintain fibre direction within acceptable bounds. This reduced variability between the intended ply angles in the FE model and the realised fibre orientations in the manufactured laminate, improving predictability of structural behaviour. The drape assessment also provided a practical indicator of lay-up difficulty, since areas predicted to wrinkle or bridge correlate directly with increased operator effort and defect risk.

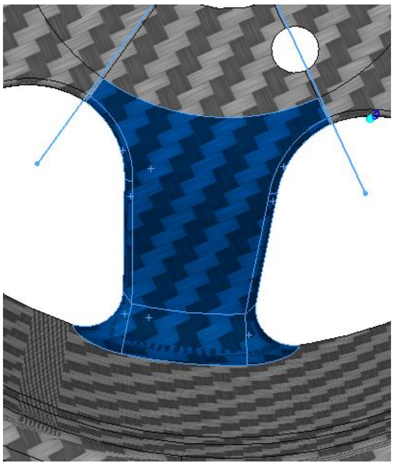

Figure 56 - 3D CAD surface of selected ply region

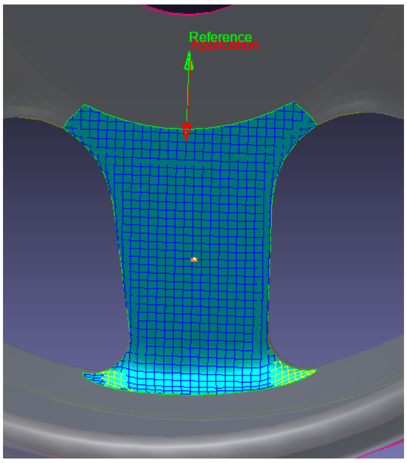

Figure 57 - drapability study, yellow region represents minor fibre distortion

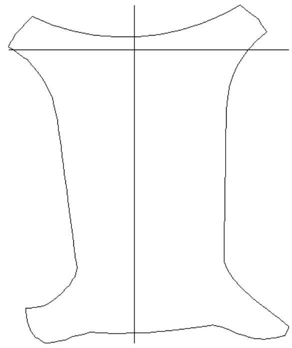

Figure 58 - 2D flattened pattern

Once ply boundaries were fixed, the 3D regions were flattened into 2D cut patterns and nested efficiently onto the available prepreg roll for cutting, ensuring consistent orientation control and minimising material waste, resulting in approximately a 56% material efficiency.

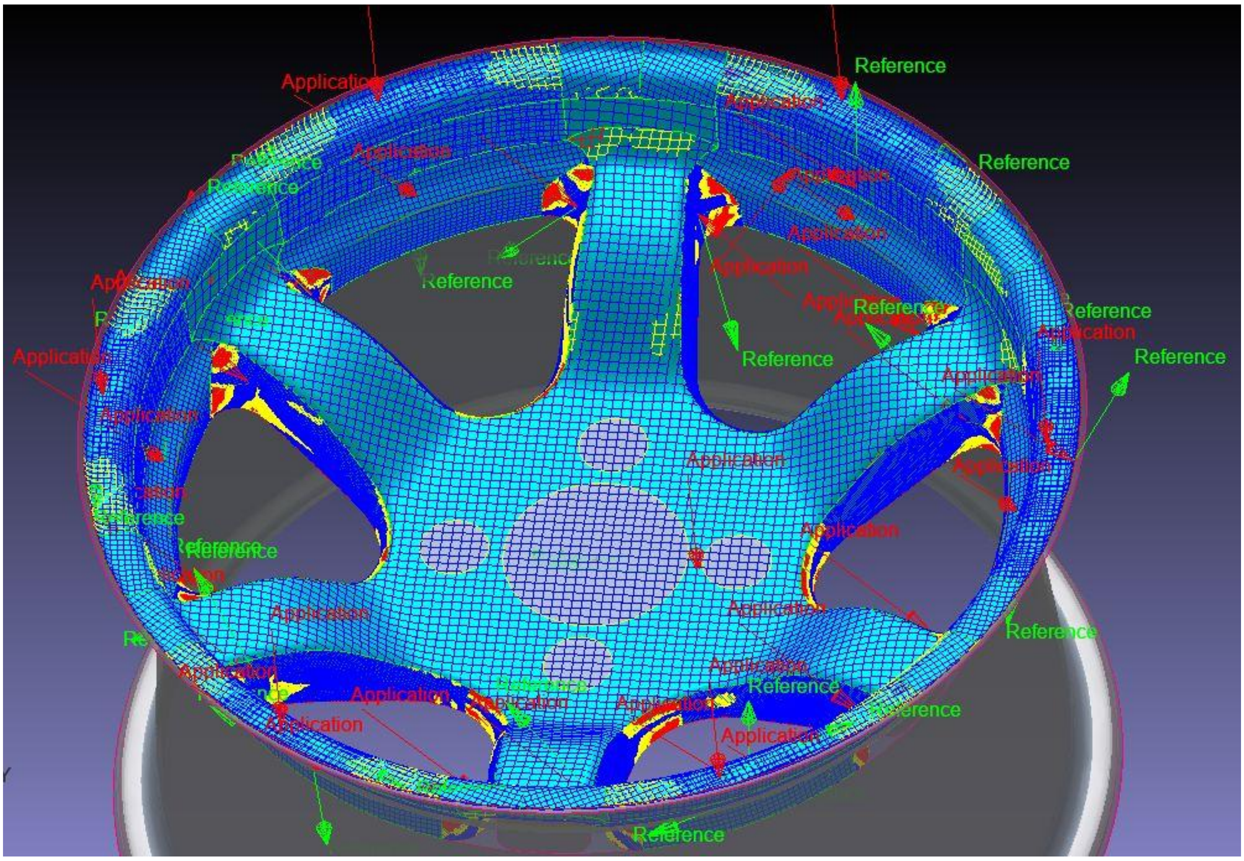

Figure 59 – All lower plies represented ready for plybook (work instruction) creation – this guides the laminator how plies should be placed and draped across the mould surface

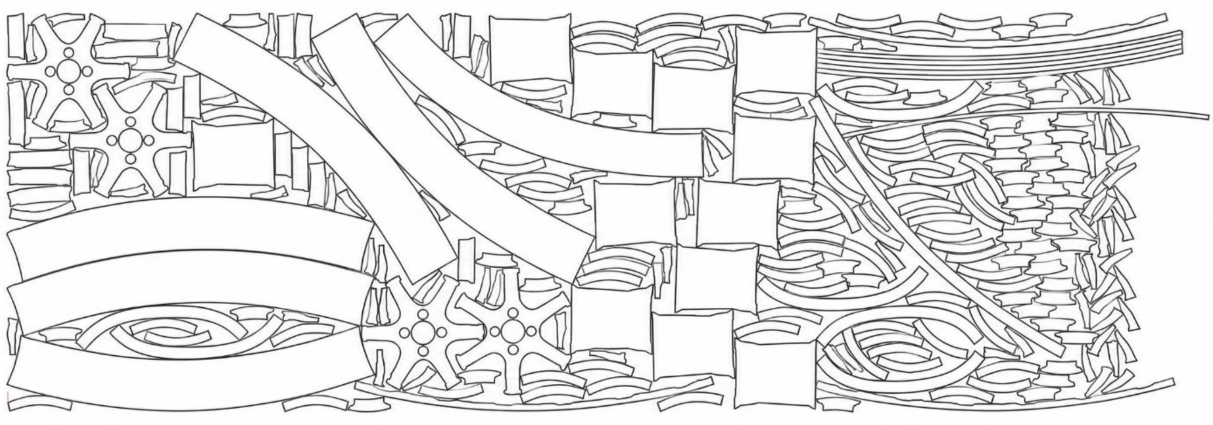

Figure 60 - 1 of 4 generated nested sheets ready for carbon fibre ply cutting

Work instructions and production documentation

Figures 57-62 show mould design and ply sets, next a formal work instruction was produced to control the build process and reduce operator-dependent variation. The work instruction captured:

- **Lay-up schedule and sequence:** which plies are placed in each mould half, their orientation, boundaries and order, including where overlaps, darts, or local reinforcements are applied.
- **Assembly and integration steps:** insertion of the metallic insert and Rohacell core, and the mould closing/bolting procedure including alignment checks.
- **Mould manufacture and preparation:** bonding strategy for the tooling-board sections, CNC machining stages, sealing/finishing operations, and release-system preparation prior to lay-up.
- **Insert definition:** CAD model, engineering drawing and machining requirements for the metallic insert, including datum features used to locate it in the mould.
- **Core definition:** CAD model and engineering drawing for the core, including tolerances required to ensure correct cavity fill and avoid local resin-rich zones.
- **Post-processing:** trimming instructions (datum references, cut lines, and tooling used) and final finishing/polishing steps required to achieve the target surface quality and dimensional specification.

3.9. Design Freeze

An artefact sheet was produced to provide traceability between the product requirements, the associated design decisions, and the evidence used to demonstrate compliance. This document was used during the design-freeze stage to ensure the wheel was released based on a structured review against defined requirements. Each requirement was recorded individually and assigned a verification method, split between virtual validation (completed prior to manufacture) and physical validation (completed post-manufacture).

Virtual checks included CAD-based mass properties, packaging and clearance verification, bead seat and interface geometry checks, alignment of critical interfaces, and finite element analysis to assess stiffness and strength against the design targets. Physical validation activities were then planned to confirm these predictions using measured component mass, dimensional inspection, tyre fitment trials, pressure retention testing, and mechanical testing where appropriate.

University of Nottingham Racing | 13" CFRP Wheel Rims — Verification Artefact Sheet

REQ-01 MASS PERFORMANCE

Minimising unsprung mass improves dynamic performance; target derived from benchmarking competing carbon race wheels against the vehicle mass budget.

REQUIREMENT	TARGET / SPEC	VALIDATION METHOD	OVERALL RESULT
Total wheel mass	**≤ 1741 g**	CAD + Physical test	✗ FAIL

VIRTUAL COMPLIANCE PROOF	
Method	CAD mass properties (SolidWorks)
Result	**1740g**
Status	Compliant

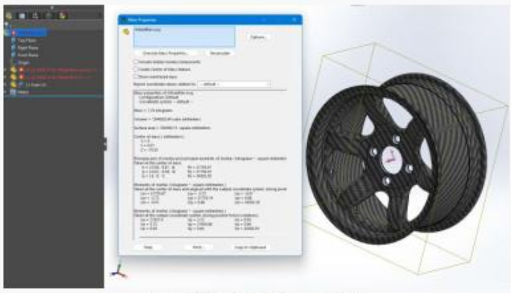

Insert FEA plot / CAD screenshot

PHYSICAL COMPLIANCE PROOF	
Method	Calibrated postal scale (±5 g)
Result	**2255g**
Status	Non-Compliant

Insert test photo / measurement evidence

NOTE *The manufactured wheel mass exceeded predictions due to additional carbon added during lamination to address voids. Post-lamination surface area calculations estimated a mass of 1,922 g, which remains below the actual measured mass of 2,255 g. This highlights a limitation in the current mass estimation approach, suggesting that either improved modelling methods or the application of a conservative blanket coefficient is required for future designs.*

26-WHE-001 | v1.0 | 2025/26 Season Page **2**

Figure 61 - Artefact sheet page 1 example, weight requirement

By explicitly linking each requirement to a defined proof method, the design-freeze milestone functioned as a formal validation gate rather than simply the point at which the CAD geometry stopped changing. The final wheel configuration was only released for manufacture once this requirement-by-requirement assessment had been completed and the planned validation route was defined.

4. Results & Discussion

Although each prototype cost thousands in materials and upwards of a hundred hours per iteration, throughout this design generation process 3 wheel rims were produced. The process established the ability to reuse tooling, reuse ply data and build experience to increase production rates, allowing the production of an initial proof of concept followed by two identical wheels. These final two rims were separated by the fact that one had a solid spoke design foam and one had the traditional C channel spoke with just carbon, this was so the concept could be directly compared further than just theoretical calculations and FEA.

4.1. Manufacturing

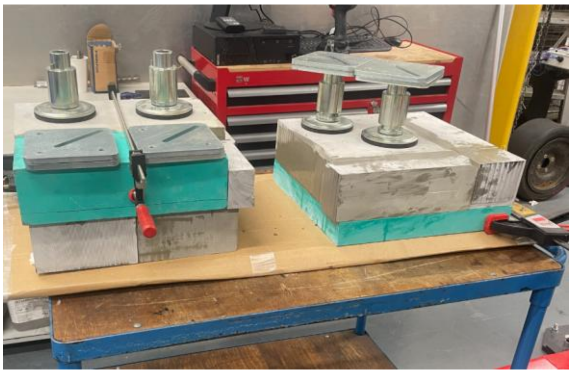

Figure 62 - gluing tooling blocks together and clamping

Figure 63 - Sanding, sealing and releasing the moulds post machining

Figure 64 - Cutting carbon plies using a 3-axis plotting cutter

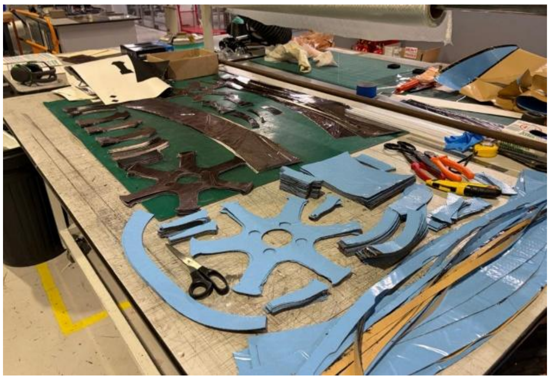

Figure 65 - All 319 plies cut and organised (both ud & woven carbon fibre)

Figure 66 - Machined foam core for variant 2

Figure 67 - machined aluminium insert - pre bond preparation

Figure 68 - Variant 1 - first layer of woven carbon

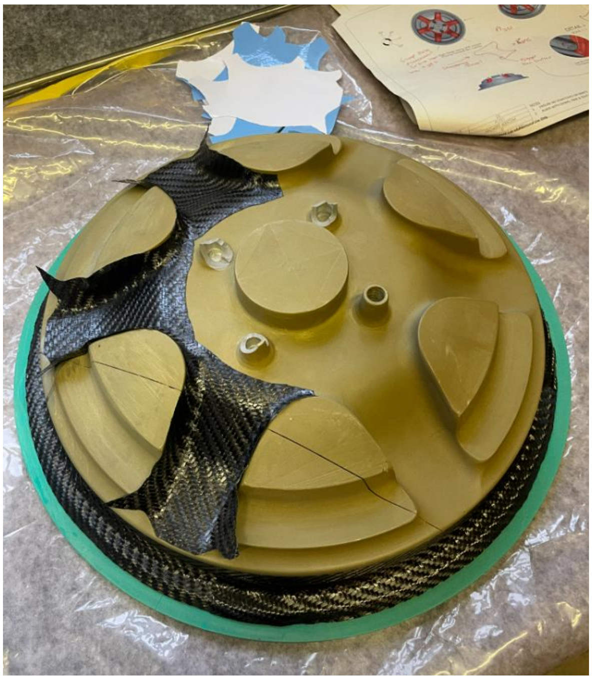

Figure 69 - Variant 1 - laminating of remaining spokes

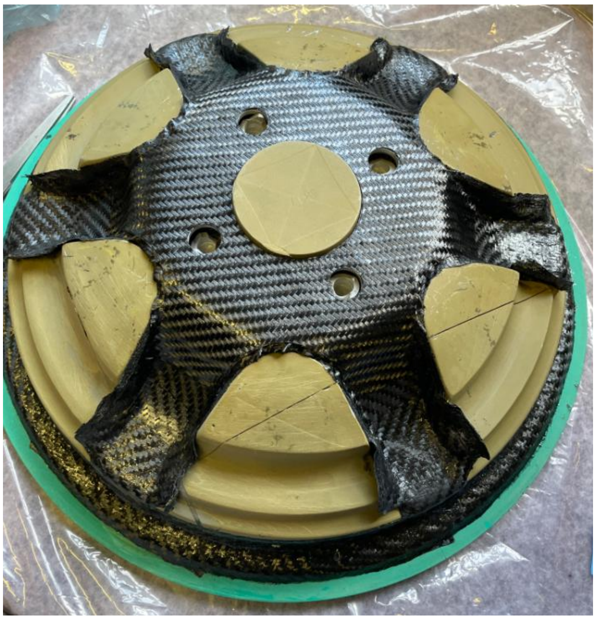

Figure 70 - Variant 1 - C-channel spokes laminated, insert placed in and laminated over (enclosed) - No Core

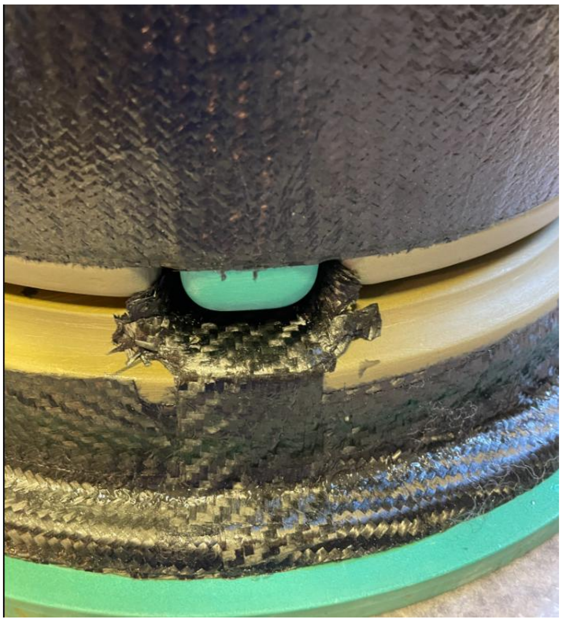

Figure 71 - Variant 1 - mould closure

Figure 72 - Variant 2 moulds, blue interchangeable mould swapped and inserted into upper mould (left hand side)

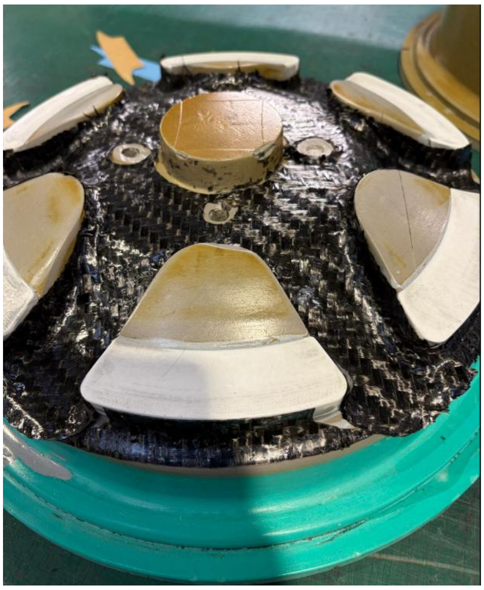

Figure 73 - Variant 2 (foam core) first layer placed into mould - Woven

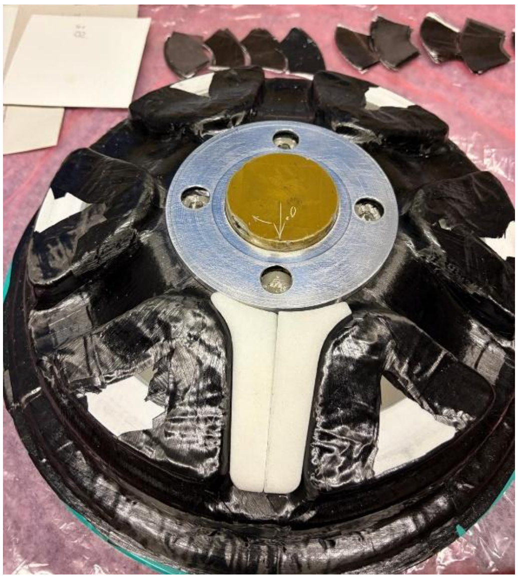

Figure 74 - Variant 2 (foam core) first foam core spoke placed alongside aluminium insert

Figure 75 – Variant 2 (foam core) placing the rest of the foam core – typically left empty with variant 1 (no foam core)

Figure 76 - First layer after combining the two mould halves

Figure 77 - Autoclave curing (3 hour dwell at 135C, 1 degree C ramp up and down)

Figure 78 - Lower mould removed, post cure

Figure 79 - Demoulded wheel, pre trimming

Figure 80 - Post cure trimming, sanding & polishing

Figure 81 - application of the Phantom Clear UV resistant coating

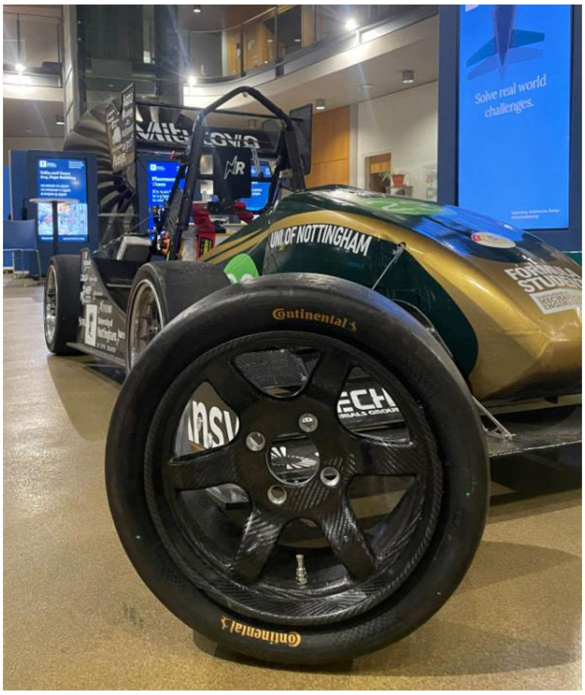

Figure 82 - Final wheel with tyre fitted infront of the FS25 race car

Figures 64 to 84 summarise the complete manufacturing process from stock material to the finished wheel. Manufacturing began by translating the CAD model into engineering drawings, DXF files and STEP geometry, which were used to manufacture tooling, machine aluminium inserts and foam cores, and cut all composite plies. These individual components were then assembled through a controlled lamination process before autoclave curing, trimming, finishing and final assembly.

Throughout manufacture, particular emphasis was placed on maintaining laminate accuracy through correct ply orientation, overlap, insert positioning and foam core fitment. While the CNC machining and automated ply cutting processes consistently achieved excellent dimensional accuracy, manual laminate assembly proved considerably more challenging than anticipated. Managing over 300 individual plies required rigorous tracking of ply order, orientation and any deviations from the laminate schedule to ensure consistency between wheel variants.

Several manufacturing lessons were identified during production. In hindsight, complete trial assemblies should have been performed before cutting the full ply kit, as minor geometric discrepancies required repeated workarounds throughout manufacture. Debulking procedures were also less effective than intended due to limited manufacturing experience, contributing to local laminate inconsistencies and becoming a key area for future process improvement. Similarly, tooling durability and accessibility require further consideration, as scratches, accidental impacts and restricted access for trimming affected surface quality and ease of manufacture.

Standard surface preparation procedures were followed before bonding the aluminium insert to minimise the risk of interfacial failure. Future work could investigate anodising the insert to further improve bond performance, although quantifying the benefit would require dedicated mechanical testing. Finally, mould closure proved more difficult than expected due to greater than predicted laminate thickness. The tooling relied on alignment dowels and vacuum pressure to achieve closure, however future iterations should incorporate bolted closure features to provide controlled clamping loads and improve laminate thickness consistency.

4.2. Testing & Validation

The artefact sheet was built up with physical testing data further proving the virtual validation, building a workflow shown in figure 85. Therefore, to prove compliance, a range of physical tests were performed to ensure compliance across a wide range of requirements. This includes dimensional and fitment checks to tyre sealing, NDT and destructive testing. Physical testing was important as simulations have no value if not correlated and although designing to standards is required, physical testing is needed to validate the design especially given the criticality of the component.

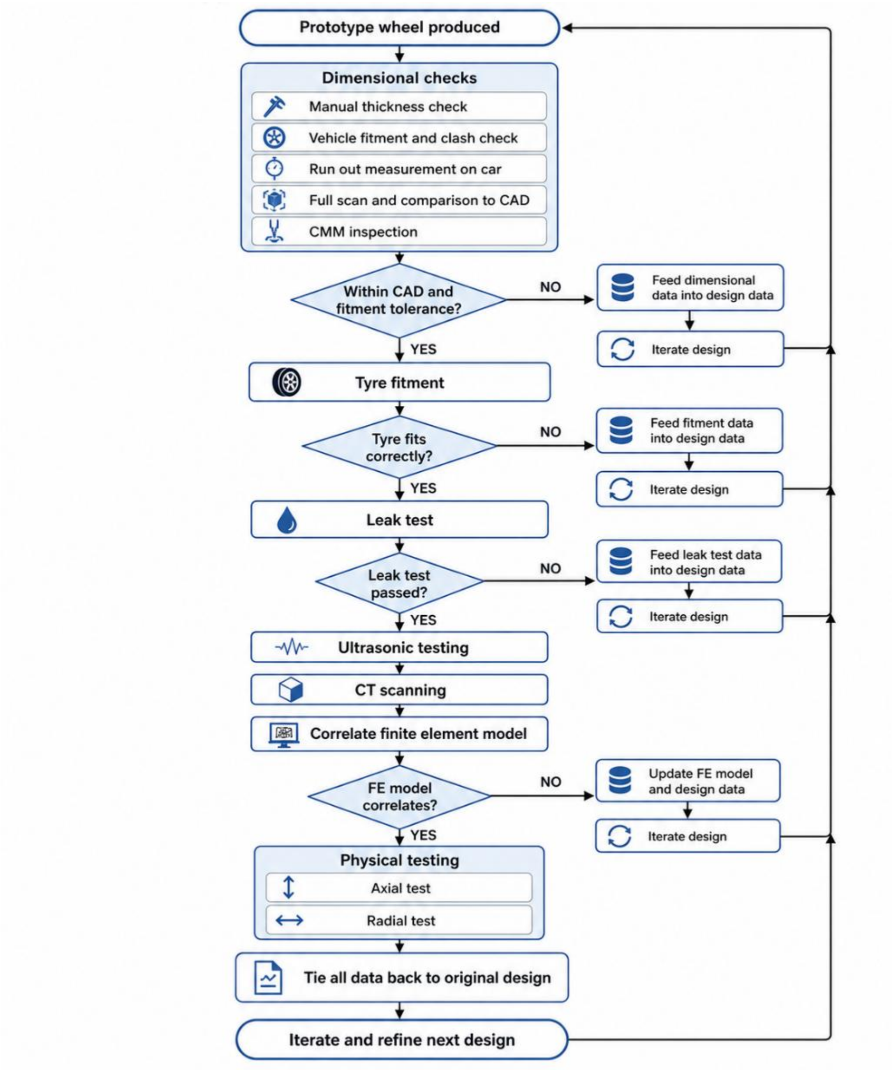

Figure 83 - Quality assurance workflow

4.3. Dimensional & Fitment

Initial dimensional verification was carried out via on-vehicle fitment. The manufactured wheel was installed to confirm the pitch circle diameter (PCD) and fastener pattern, verify that all bolts could be torqued without interference, and ensure the mating faces seated correctly against the CAD-defined interfaces. Clearance checks around adjacent components showed no clashes, confirming the assembly mounted as intended. The only notable deviation was laminate thickness, which was approximately 30% higher than expected; this was fed back into the design loop and is likely attributable to local wrinkling, insufficient debulking, or uncertainty in the pre-manufacture thickness estimate. Fitment and inspection methods are shown below in figures 86-95 with results shown in tables 9 and 10.

Figure 84 - Fitting wheel and tyre assembly onto the FS25 racing car

Figure 85 - Measuring barell thickness

Furthermore, the wheel was spun and checked for runout with a dial indicator pressed onto the internal surface of the inner and outer beads. This was key as a requirement was to ensure runout was limited to 400 microns. The outboard bead seat was within tolerance, but the inboard bead seat was not, showing 1.43 mm runout. This points to upper–lower mould misalignment during cure and is a key issue to address in the next iteration.

Figure 86 - CFRP wheel fitted to the front suspension for run-out measurement

Figure 87 - Close up showing dial indicator sweeping inner bead surface (external surface is too rough for useful readings)

Table 10 - total indicated runout values from measuring baseline (aluminium) and new (CFRP) rims.

Wheel	*Total Run-out (inboard) / mm*	*Total Run-out (outboard) / mm*
Aluminium	0.37	0.22
Variant 2 (foam core)	1.43	0.36

Scan data and physical measurements were used to verify key properties and validate the manufacturing process. Initial checks were completed with hand tools as shown above, but for critical locating diameters this approach lacked coverage and accuracy, a blue-light 3D scan was used to compare the manufactured part directly against the CAD model. Following the common metrology guideline that measurement accuracy should be ~10× tighter than the tolerance being assessed, verifying a 600µm runout would require measurement capability on the order of 60µm, which is achievable with blue-light scanning.

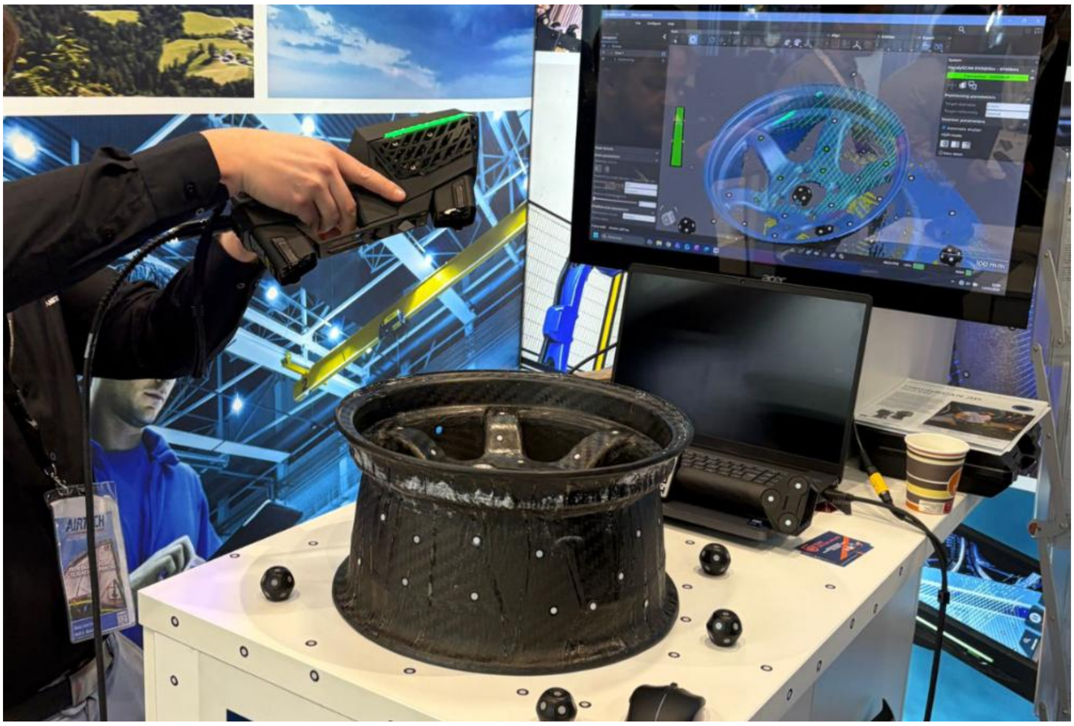

Figure 88 - 3D blue light scanning of Variant 2 CFRP wheel rim for dimensional inspection

The scan data was processed into a 3D mesh that could be aligned to the CAD nominal geometry to quantify local deviations. This enabled a full-field inspection of the manufactured rim, identifying regions of warpage introduced during cure, areas that were clearly out of tolerance, and features that deviated from the intended design intent. The deviation maps provided empirical evidence that complemented datasheets, calculations, and pre-manufacture estimates, which can only capture part of the as-built behaviour. This measurement-led insight was therefore fed directly into the design loop to refine assumptions on cured laminate thickness, improve mould dimensional accuracy, and reduce uncertainty in subsequent iterations.

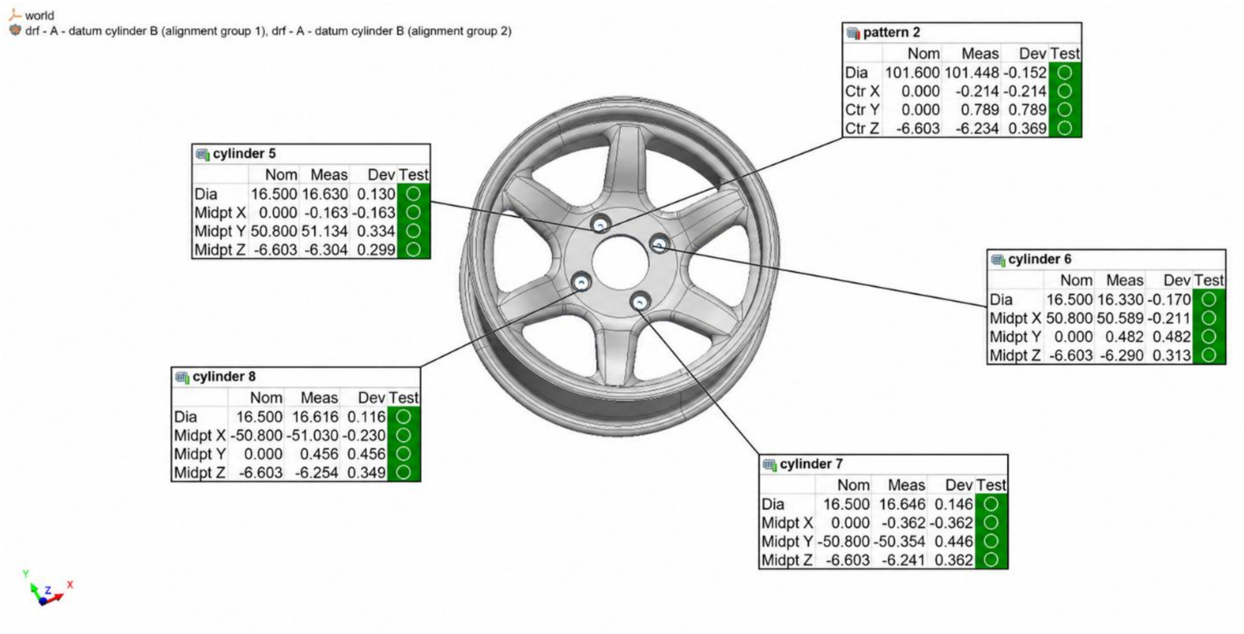

Figure 89 - Inspection report showing PCD of bolt holes being to spec allowing for proper mating between the two assemblies

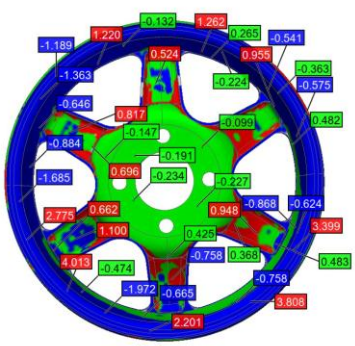

Figure 90 - Rear image depicting variation in the model, showing barrel is overall 1mm smaller than expected

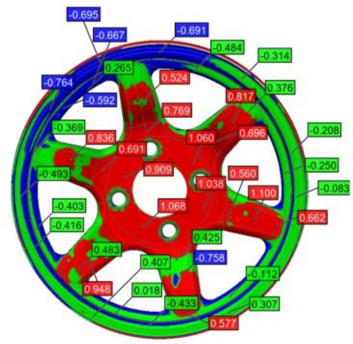

Figure 91 - Front image depicting variation in the model, the front face is more outboard than expected

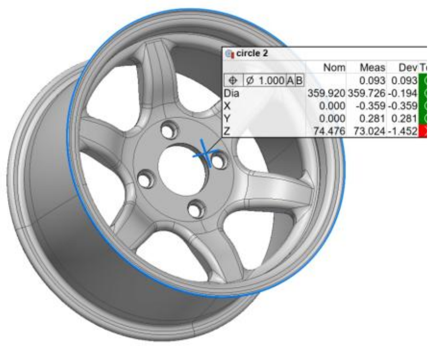

Figure 92 - Scan data showing runout of the inner bead relative to the outer bead to be approx. 1.45mm, similar to the measured runout

Table 11 - Key dimensions of interest during metrology

Feature	**CAD / mm**	**Reality / mm**	**Deviation / %**
Thickness of bead	6.23	7.8	+20%
Thickness of barrel	4.2	4.8	+12.5%
Outer diameter	322	326	+1.23%
PCD of bolt holes	101.6	101.448	-0.15%
Angle of bolt hole cones / degrees	60	55	-9%
Overall surface tolerance +-0.5mm			+68.5%

Overall, deviations were mainly driven by poor laminate thickness control, likely from lay-up/debulking and resin distribution variability, which increased the outer diameter and created tyre-fitment risk. Excessive inboard bead-seat runout was most consistent with upper–lower mould misalignment during cure; the lower surface form was good, indicating the lower tool was sound and alignment control of the upper tool is the priority. A further issue was an incorrect bolt-hole cone angle (a straightforward design error), while the bore and PCD locations relative to the gearbox were as intended.

4.4. Tyre Fitment, Sealing & Balancing

Tyre-related dimensional validation was also treated as a critical fitment check. The primary objective was to confirm that the tyre could be installed and removed from the rim without damage, and that the bead seated correctly to enable inflation and sealing. This represented a higher-risk validation activity because tyre fitment could not be fully confirmed prior to manufacture; adherence to the relevant ETRTO rim and bead-seat geometry guidance was therefore the main mitigation available at the design stage.

Following manufacture, a valve stem hole was drilled and fitted to allow inflation. The tyre was then mounted using a tyre-changing machine, gradually working both sidewalls onto the rim. A race tyre of the same specification as that intended for the event was used to ensure the validation was representative. Next the tyre was checked for balance and weights we're added to correct the 15g in balance, this process is shown in figures 97-102.

Figure 93 - Valve stem fitted

Figure 94 - Tyre fitment (205/470R13 34M slick) using a tyre changing machine

Figure 95 - Tyre fit and inflated onto rim - post leak test - dunk tank seen in background

Figure 96 - Wheel and tyre assembly on wheel balancer

Once mounted, the tyre was inflated; upon exceeding approximately 35 psi, an audible bead “pop” indicated that the bead had seated correctly. After successful seating, pressure retention was assessed as an initial indication of sealing performance. The tyre was inflated to 37.5psi and left for seven days. Pressure was recorded at 24-hour intervals and reduced to 36.5psi, losing 1 psi across 168 hours (0.006psi/hr) – passing the ≤0.1 psi/hr target.

Figure 97 - First day (1) of pressure test - reading 37.5 psi

Figure 98 - Final day (7) of pressure test - reading 36.5psi

4.5. NDT - Ultrasonic & CT scanning

Given that composites are layered structures, it is essential to identify subsurface defects such as cracks, voids, and delaminations. As the wheels are safety-critical components, their internal integrity must be understood, particularly at joining interfaces – such as the bond between the insert and the composite.

This inspection should be completed prior to mechanical testing, as loading can initiate or extend cracks and therefore obscure the true manufacturing quality. Defect mapping also helps anticipate likely failure modes and interpret where and why damage initiates. Two methods were therefore used: ultrasonic inspection and X-ray computed tomography (CT).

Ultrasonic

Ultrasonic testing provides a low-cost screening tool by transmitting sound waves through the component and analysing reflections at material boundaries. Changes in acoustic impedance, such as those caused by entrapped air, produce distinct echoes - enabling detection of inconsistencies within the laminate shown in figures 103-105.

Figure 99 – Ultrasonic test setup with probe detector

Figure 100 - Result from ultrasonic testing

The results are shown in the figure below. The right-hand panel displays the raw ultrasonic response: after the pulse is transmitted, the system records returning reflections. To aid layer identification, a finger was placed against the rear face of the laminate and lightly tapped, producing a clear pulsating band in the signal corresponding to the back-wall/interface location.

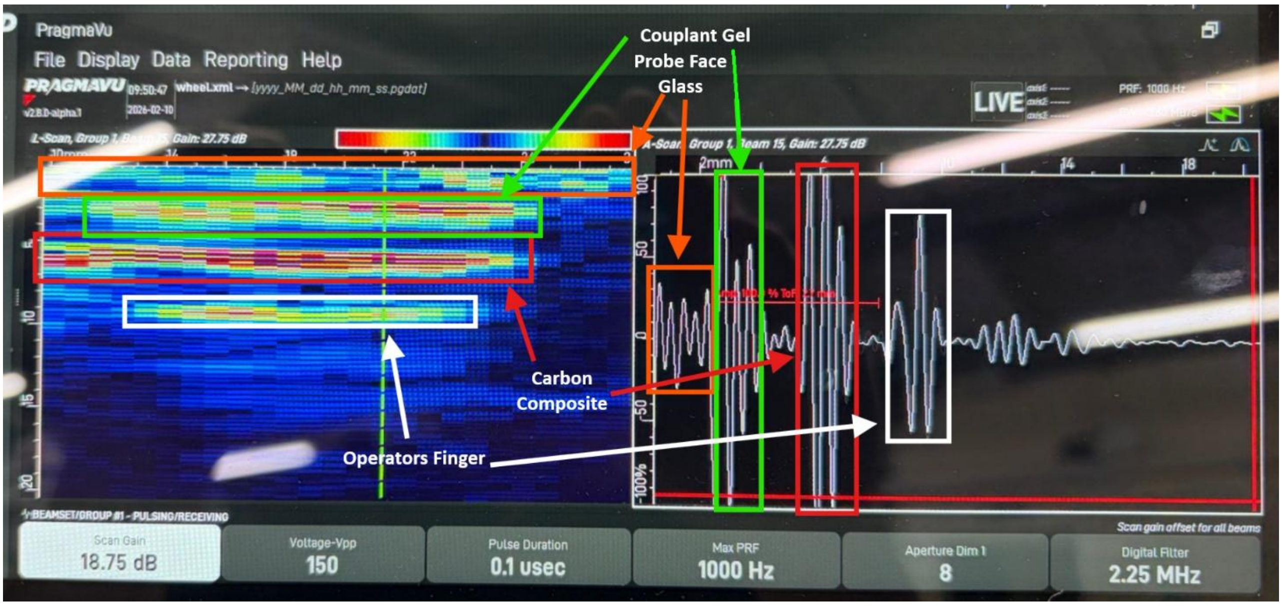

Figure 101 - Ultrasonic testing - zoomed in snippet

As shown on the left-hand side, the software provides a graphical view of the detected layers. The first band corresponds to the transducer face, followed by the couplant gel applied to ensure consistent contact over uneven surfaces. The third layer (red) is the carbon composite, which produced a strong reflection, indicating minimal energy loss to gaps or voids. The operator's finger is visible as the final white band.

Overall, ultrasonic testing confirmed good compaction in large, relatively flat regions such as the barrel and the metal–composite interface. However, the flat probe geometry and limited setup resolution made it less suitable for complex features such as the flange and spokes, which required further investigation.

Computed Tomography

To address these limitations, X-ray computed tomography (CT) was used as an alternative inspection method. Unlike ultrasonic testing, CT provides higher-fidelity volumetric data and enables direct visualisation of internal geometry, allowing complex regions such as the flange and spokes to be assessed for voids, cracks, and interfacial defects. However, this improvement comes with trade-offs, the technology is significantly more expensive, typically requires longer acquisition and post-processing times. This process and its results are shown throughout figures 106-110.

Figure 102 - Wheel going into the CT scanner

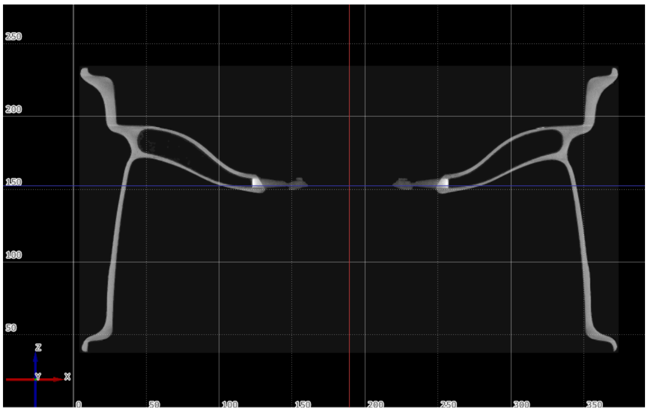

Figure 103 - CT scan results

In the reconstructed image, higher-density, well-consolidated material appears bright, whereas low-density regions appear dark. Localised dark features within the laminate therefore indicate voids or interlaminar gaps, which are potential stress concentrators and can reduce local stiffness and strength.

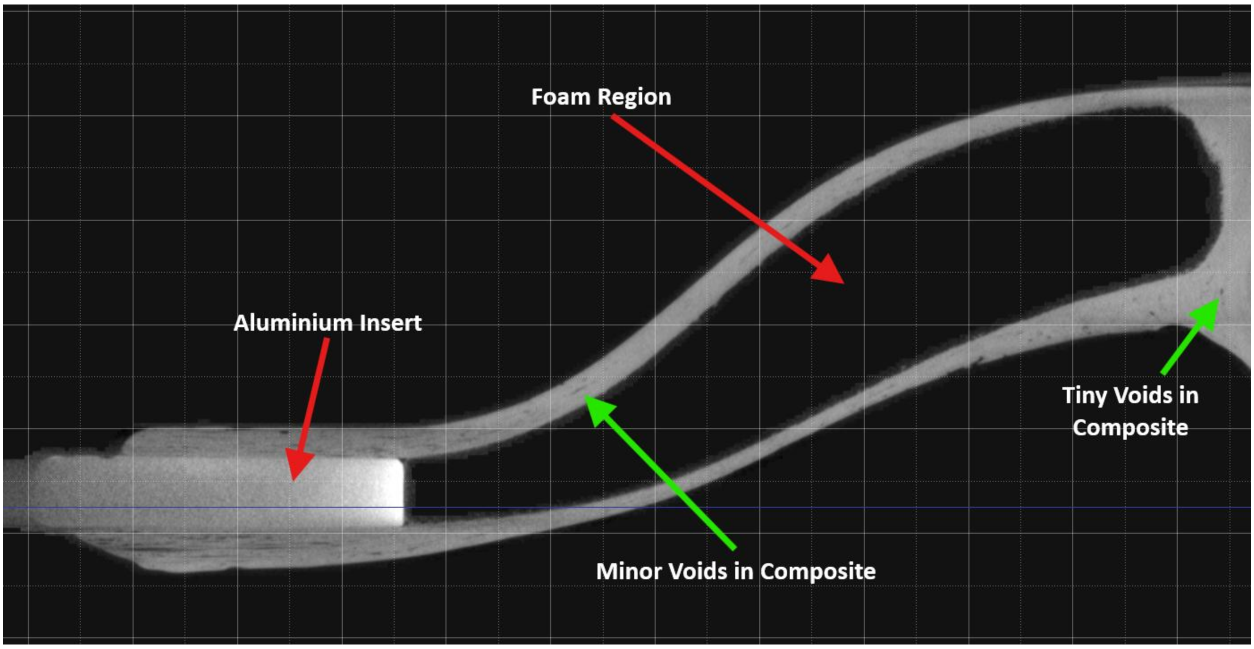

Figure 104 - Close up section of CT scanning results on Variant 2 (with foam)

Figure 108 shows a CT cross-section through the spoke–insert interface. The aluminium insert exhibits continuous contact with the surrounding laminate, indicating a sound joint with no gaps.

Consolidation around the foam core appears uniform, with consistent wall thickness through the section. However, small, isolated voids are visible within the composite, particularly toward the outer span. Although minor, these defects could potentially act as stress raisers and initiate microcracks under cyclic loading.

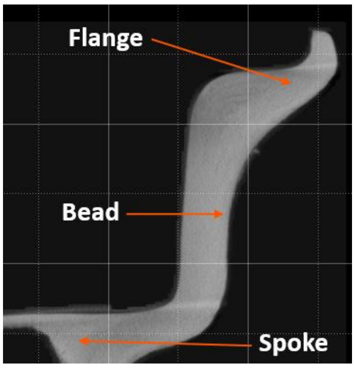

Figure 105 - Lower mould external barrel

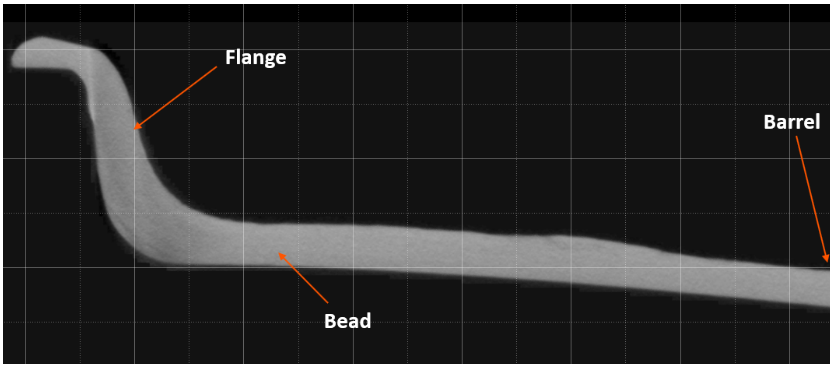

Figure 106 - Upper mould external barrel

Overall, NDT indicates that the wheel cured and consolidated well in the regions most accessible to ultrasonic testing, with CT scans further confirming a consistent external laminate along the flange, bead, and barrel. The aluminium–composite interface also appears well bonded, with no obvious interfacial gaps. While CT revealed small, localised voids within parts of the laminate, these defects are minor and spatially isolated; nevertheless, they remain relevant as potential stress raisers that could promote crack initiation under cyclic loading. This is most likely linked to wrinkles in the UD plies observed during lay-up and should be fed back into the ply-selection loop to mitigate recurrence in future designs.

4.6. Correlation

Mechanical testing was conducted to approximate representative track loading by constraining the wheel in a range of orientations and applying controlled forces. Before these results could be used as evidence of compliance, the FE simulations that informed key design decisions were first validated against the physical test data to establish confidence in their predictive accuracy.

A repeatable benchmark test was defined with matched geometry, boundary conditions, and loading in both FEA and experiment. An axial stiffness test was chosen because it provides a simple, well-defined load path while avoiding tyre-induced non-linearities and bead-seat contact uncertainty.

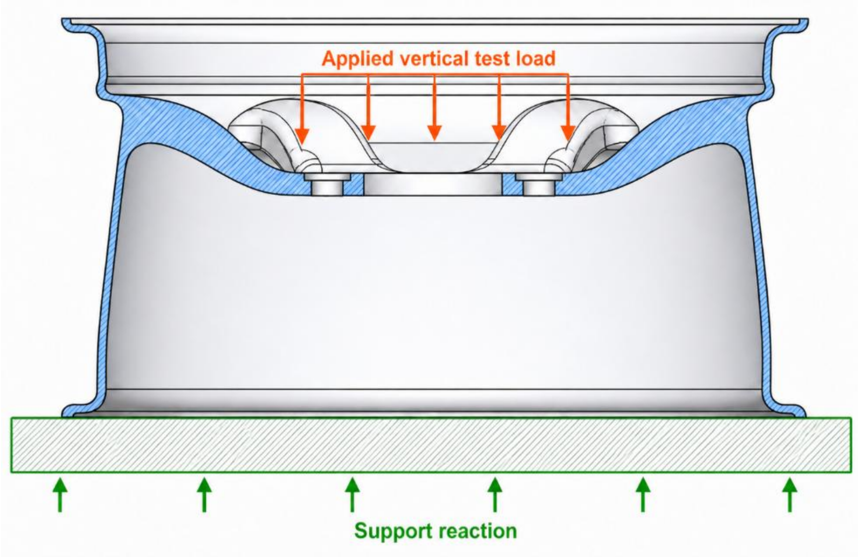

Figure 107 - Axial load test diagram

As shown in Figure 111, the axial stiffness configuration was symmetric with respect to the spoke layout, resulting in a comparatively uniform stress distribution and reducing sensitivity to local asymmetries in fixturing. A physical test was carried out to validate the model. The test was completed on a tensile/compression testing machine which applied a compression load of 10kN on the centre, compressing the structure against the base plate, demonstrated in figures 112-114.

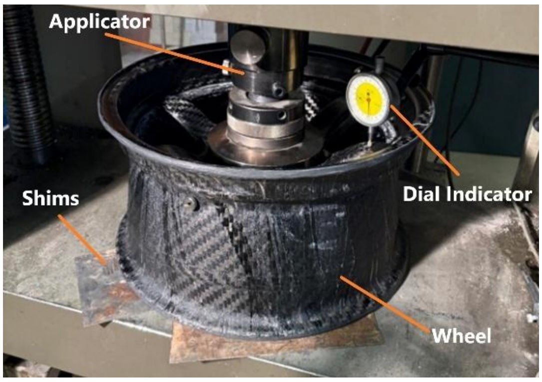

Figure 108 – Variant 2 (foam) wheel rim under axial load conditions with dial indicator (shims to limit movement)

Figure 109 - Variant 1 (no core) under axial loading

Preloaded to 1kN, the wheel was shimmed to eliminate the influence of local surface irregularities at the rim lip and to ensure consistent contact with the support platen. This approach removed the initial non-linear "settling" behaviour and improved repeatability by promoting a predominantly linear load–deflection response.

Deflection was measured using a dial indicator positioned at multiple locations on the wheel to capture both global and local deformation behaviour. These measurements were then compared directly against the corresponding displacement outputs extracted from the finite element model at the same locations.

Figure 110 - Close up shot of test rig, dial indicator measuring spoke deflection

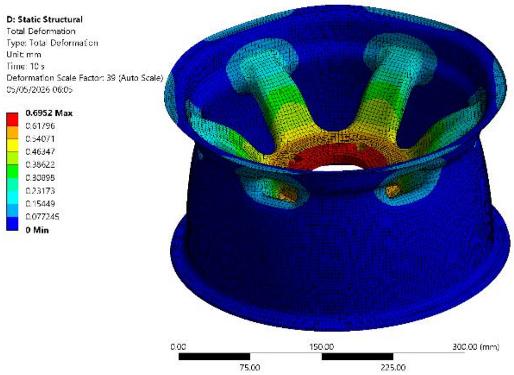

Figure 111 - FEA model representing an axial load of 10kN, results show are total deformation

Table 12 - Results from FE correlation of axial stiffness

Data (Variant 2 – foam core)	FEA Simulation	Physical Test	Discrepancy
Max Displacement / mm	0.141	0.146	~3.42%
Stiffness / N/mm	70922	68493	

As seen in Figure 115 and table 11, discrepancy of 3.42% was recorded in the axial test. This remaining discrepancy between the FE predictions and the experimental response is likely due to manufacturing variability and measurement uncertainty, particularly from manual lay-up causing local deviations in ply placement, fibre orientation, resin distribution, and laminate thickness that are not captured in the idealised model. Despite these limitations, the relationship is sufficient to use the model predictively in subsequent design iterations and to explore more complex load cases with increased confidence.

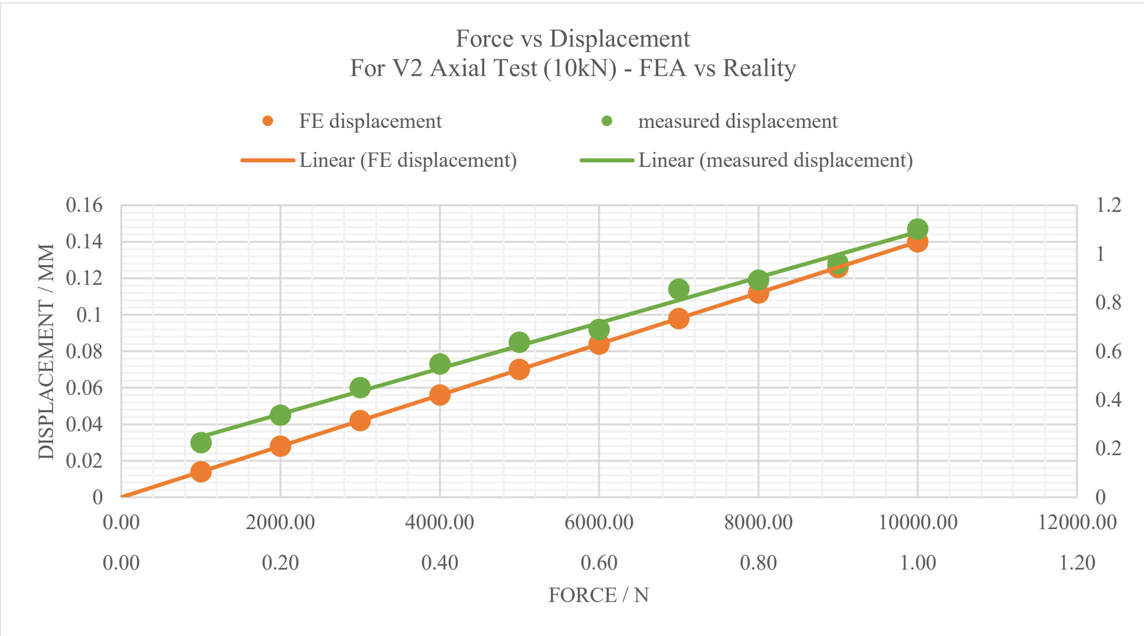

Figure 112 - Variant 2 correlation data for axial stiffness compared to FEA

The axial stiffness benchmark showed close agreement between FEA and test (0.141mm vs 0.146mm at 10kN, ~3.4%), giving sufficient confidence to use the model as a predictive tool for subsequent design iterations and more complex load cases.

4.7. Mechanical Testing (Foam Vs No Foam)

Mechanical testing then shifted from model correlation to concept verification, with the aim of quantifying the structural benefit of incorporating a foam core relative to a monolithic laminate. Both the initial analytical estimates and the FE results predicted a substantial stiffness gain for the cored concept (≈76% and ≈71%, respectively). Using the same 10kN axial setup as before, data was collected for both wheel rims to provide a clear, evidence-based recommendation on which architecture should be prioritised in future design iterations.

Table 13 - Variant 1 vs Variant 2 deflections, axially at 10kN

Design	*Deflection @ 10 kN (mm)*	*Change vs C-Section*
Aluminium	0.370	
V1 (no core)	0.252	—
V2 (foam core)	0.147	−42% deflection ≈ +72% stiffness

Under a 10kN axial load, the foam-cored spoke (variant 2) deflected 0.147 mm, compared with 0.252 mm for the no-core C-section (variant 1) (and 0.370 mm for the aluminium baseline). Relative to variant 1, variant 2 achieves a 42% reduction in deflection, equivalent to an approximately 72% increase in axial/bending stiffness. Although variant 2 is 167 g (~8%) heavier than variant 1, primarily due to the added Rohacell IG110 foam core, its stiffness gain is large enough to indicate a clear improvement in stiffness-to-weight (specific stiffness) performance.

Table 14 - final comparison between concepts foam vs no foam in the spokes

Metric	*Result*
Bending stiffness improvement	+71%
Mass increase	+8% (+167 g)
Specific stiffness improvement	+59%
Material cost increase	+10%
Labour increase	+39% (+9 hours)
FEA accuracy	Within 5%

A +71% bending stiffness gain was achieved with the foam-core concept for a relatively small penalty of +8% mass (+167 g), translating to a +59% improvement in specific stiffness. The trade-off is primarily practical: material cost increased by ~10%, and manufacturing effort increased by ~39% (~9 hours) due to core machining and the more complex lay-up workflow. Overall, the stiffness improvement is a strong value-add in a competition context, where marginal performance gains often require disproportionate investment, supporting the foam-core architecture as the preferred concept for future iterations. Finally, the modelling approach was validated, with FEA within ~5% of test data, confirming the measured stiffness gains are consistent with prediction.

4.8. Virtual Tests

Some tests, while theoretically required, were judged to be low value within the project scope and risked consuming time without improving outcomes. These were therefore addressed virtually using calculations and engineering judgement to confirm they would not compromise the design.

Thermal exposure is widely cited as a constraint on composite wheel adoption in high-energy motorsport (e.g., Formula 1) - however, a dedicated thermal analysis was not performed because 2025 physical testing recorded a maximum brake-disc temperature of 90 °C, placing expected service temperatures well below the resin system's 180 °C cure specification and providing an approximate 2× margin at this design stage, shown in figures 120 and 121.

Figure 113 - 21/09/2025 thermal imaging (via FLIR) post endurance test running

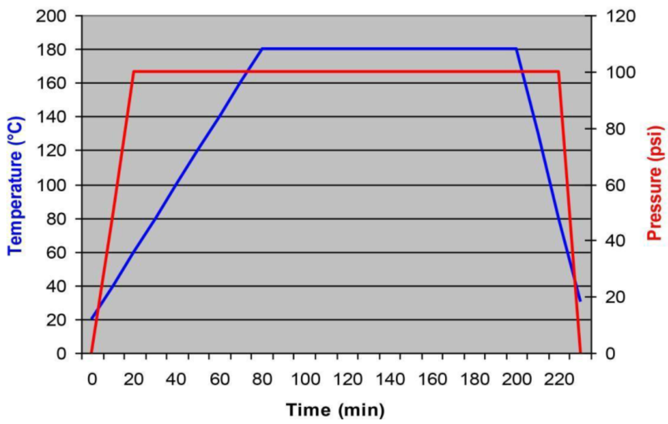

Figure 114 - Final component cure cycle, resin system dwell at 180C

UV degradation was identified as a potential failure mechanism for the wheel's surface finish. To mitigate this risk, the wheel was coated using Phantom Clear, a UV-resistant clear coat. This coating provides both an improved visual finish and a protective barrier that reduces sunlight-induced degradation over the service period.

4.9. Final Discussion

Table 7 summarises the outcomes of the three rim iterations and provides a quantitative comparison against the aluminium baseline. The design process progressed from demonstrating feasibility (V1), to pursuing maximum performance and understanding its resource implications (V2), and finally to isolating the effect of the foam core while demonstrating repeatable manufacture (V3).

Table 15 - Final generation 1 key statistics

Property (per rim)	*Aluminium (Baseline)*	*Version 1 (proof of concept)*	*Version 2 (foam spokes – V2 layup)*	*Version 3 (non foam spokes – V2 layup)*
Mass / g	3482	1252	2362	2255
Axial stiffness N/mm	27027	18518	71428	41666

Time to manufacture / hrs	6	28	51	36
cost / £	339	464	689	613

Wheel 1 (proof of concept) demonstrated that a composite rim could be manufactured and integrated, achieving a large mass reduction relative to aluminium (1252 g vs 3482 g). However, axial stiffness remained below the baseline (18,518 N/mm vs 27,027 N/mm) and manufacturing effort was still high (28 h), prompting further iteration.

Wheel 2 introduced a foam core with unidirectional reinforcement, delivering the highest axial stiffness (71,428 N/mm) and surpassing the aluminium rim. This performance came with the largest manufacturing burden (51 h) and increased theoretical cost, highlighting a clear performance–resource trade-off.

Wheel 3 retained the Version 2 lay-up intent but removed the foam core to isolate its contribution. Stiffness remained above the aluminium baseline (41,666 N/mm) with reduced manufacturing time (36 h). Comparing V2 and V3 shows the foam core provides a substantial stiffness gain (71,428 vs 41,666 N/mm) at the expense of additional labour and cost, while V3 also suggests improved repeatability for future batch manufacture.

Figure 115 - All 3 version 1 wheels, wheel 1 to 3 from left to right

Generation 1 established the feasibility of manufacturing and integrating a composite rim but also highlighted several priorities for a second-generation design. Dimensional verification via fitment was acceptable overall; however, radial runout approaching ~700µm, while usable, should be reduced through tighter tolerance control and more consistent tooling and process control.

Manufacturing time also requires significant reduction - on the order of tens of hours per wheel is not scalable to a set of four - motivating simplification of the plybook, clearer process documentation, and design changes that make lay-up more repeatable. Surface quality and laminate consistency should be improved through more robust debulking and improved tool preparation, with particular attention to controlling laminate thickness variability and placement.

Structurally, there remains headroom to improve stiffness and/or reduce mass because the current architecture is not yet fully optimised for stiffness and weight. Finally, the next validation phase should prioritise practical mechanical testing to build a stronger evidence base for concept selection and to progress towards full standard-based verification, alongside strengthening the flange region to improve repeatability of tyre fitment.

Generation 2

Generation 2, gen 2, built directly on the validated gen 1 concept, addressing the main practical limitations by improving tolerance control and dimensional repeatability, optimising the geometry to increase stiffness, and streamlining the manufacturing route to reduce build time to under 50% of the original process. Gen 2 is not discussed in detail in this dissertation because the primary aim was to establish a manufacturable carbon-fibre wheel design and structurally validate it against an aluminium baseline, which was successfully achieved using gen 1; nevertheless, the same development workflow and validation principles were applied to gen 2, and its outcomes informed subsequent iteration work. A second paper will be written on the second iteration of wheels, focussing on streamlining and optimising alongside ensuring consistent quality throughout production.

Figure 116 - All 3 generation 2 wheels, wheel 1 to 3 from left to right

5. Conclusions

This project developed, manufactured and validated a 13-inch carbon fibre reinforced polymer (CFRP) wheel rim for Formula Student, targeting reduced unsprung/rotational mass while maintaining stiffness, fitment and safety. The work followed a complete engineering cycle: requirements capture (FSUK legality, ETRTO geometry and vehicle packaging), concept selection, parametric CAD, ply-by-ply composite FEA in ANSYS ACP, tooling and prepreg manufacturing, and a structured inspection and test programme. Load cases were defined and cross-checked using theoretical calculations, lap time simulation outputs and track-derived IMU data to ensure representative inputs for analysis and validation.

Manufacture and integration feasibility were demonstrated through iterative prototyping, with metrology and on-vehicle fitment confirming overall compatibility with the vehicle package.

Dimensional inspection also highlighted key process-driven deviations (notably laminate thickness variation and inboard bead-seat runout), enabling targeted feedback into the design and tooling loop. Tyre fitment and pressure retention were successfully demonstrated, with the assembly meeting the project leakage target over a seven-day test. Internal quality was assessed using ultrasonic inspection and CT scanning, indicating generally good consolidation and a sound insert–laminate interface, while identifying small, localised voids for future process refinement.

The analysis workflow was validated through an axial stiffness correlation test, showing close agreement between FEA and experiment (~5%), providing confidence in the predictive model. Physical concept testing then quantified the structural benefit of foam-cored spokes, delivering a 42% reduction in axial deflection at 10kN (≈72% stiffness gain) for an ~8% mass increase, confirming the performance–resource trade-off. Overall, the project's key contribution is a repeatable, evidence-based methodology for composite wheel design and validation, combining correlated simulation with practical inspection and testing suitable for a student motorsport environment.

6. Future Work

Generation 2 delivered a major increase in strength and stiffness, but dimensional stability issues and a labour-intensive build process limited practicality. Gen 3 will retain the gen 2 performance gains, while restoring the key gen 1 functional requirements, with further design-for-manufacture simplifications, improved unidirectional optimisation, and tighter control of lamination and bonding to improve repeatability.

Once requirements are met, gen 3 will be batch-manufactured for late-June track testing. Validation will use strain-gauge instrumentation and full batch QA (blue-light scanning, CT inspection, stiffness testing), with leak testing to confirm readiness for the Silverstone competition in July.

A third paper will be written on generation 3 and its validation with real track testing, correlation and detailed modelling techniques alongside overall lessons learned from the project.

7. Acknowledgements

For a project completed on just £100, this work would not have been possible without the generosity and support of many people. Their time, resources, and patience were generously given, thank you to:

- The University of Nottingham Racing (UoNRacing) team, for supporting me throughout the project and giving me the opportunity to pursue such a challenging (and exciting) project.
- Surojit Sen, for support and guidance at every step.
- Liam Sprake and the Composites Team, for guidance and autoclave access.
- Nick Warrior, Mikhail Matveev, and Mike Johnson, for teaching me the fundamentals of composites.
- Ali Palmer, for support with physical mechanical testing.
- Sean Turner, for help developing concepts and assisting with last-minute fixes.
- The L2 Central workshop team, for producing high-quality metallic parts.
- Jason Young, for 3d printing concepts and scanning prototypes.
- Alex Jackson-Crisp, for workshop access to machine metallic parts.
- Michael Doherty and the ANSYS Team, for introducing and guiding me through ANSYS ACP.
- Ares Kretis and the Anaglyph Team, for providing laminate design software/tools.
- Freya Baker and the EmKay Team, for supplying Rohacell core material.
- Richard Bell and the ZEISS Quality Team, for conducting CT scanning of the rims.
- Simon Baily and the Mitutoyo Team, for carrying out CMM inspection of the rims.
- Lewys Morley and the FARO Team, for scanning and providing point-cloud CAD models.
- Chris Marsden and the Pentaxia Team, for technical discussions and production equipment access.
- Martin Gouldthorpe and the Vac Innovations Team, for supplying consumables free of charge.
- Pete Wilson and the Syensqo Team, for supplying prepreg carbon fibre.
- John Miller and the Base Materials Team, for supplying epoxy tooling block.
- Nick Henry and the CarbonThreeSixty Team, for guidance on wheel rim design and production.
- Joshua Aigbotsua and the Baugher and Weedon Team, for ultrasonic testing of the wheel rims.
- And many others who contributed their time, expertise, and resources - thank you.

8. References

[1] IMechE. FSUK 2025-26 Rules

[2] W. F. M. a. D. L. Milliken, "Race Car Vehicle Dynamics," *Warrendale, PA, USA: SAE International,* 1995.

[3] D. Seward, *Race Car Design*. 2014.

[4] C. E. Harris, Starnes, J.H. and Shuart, M.J., "Advanced durability and damage tolerance design and analysis methods for composite structures: Lessons learned from NASA technology development programs. NASA Technical Memorandum.," 2003.

[5] A. V. Guimaraes, P. C. Brasileiro, G. C. Giovanni, L. R. O. Costa, and L. S. Araujo, "Failure analysis of a half-shaft of a formula SAE racing car," *Case Studies in Engineering Failure Analysis,* vol. 7, pp. 17-23, 2016/10/01/ 2016, doi: https://doi.org/10.1016/j.csefa.2016.05.002.

[6] X. Yan, N. Zhang, X. Guo, and H. Wang, "A coupled FE-FFT multiscale approach for predicting mechanical responses and failure behavior of CFRP composite materials and structures," *Engineering Fracture Mechanics,* vol. 331, p. 111699, 2026/01/22/ 2026, doi: https://doi.org/10.1016/j.engfracmech.2025.111699.

[7] C. Benini, M. Gadola, D. Chindamo, S. Uberti, F. P. Marchesin, and R. S. Barbosa, "The influence of suspension components friction on race car vertical dynamics," *Vehicle System Dynamics,* vol. 55, no. 3, pp. 338-350, 2017/03/04 2017, doi: 10.1080/00423114.2016.1267370.

[8] R. Real, C. Snider, M. Goudswaard, and B. Hicks, "DIMENSIONS OF KNOWLEDGE IN PROTOTYPING: A REVIEW AND CHARACTERISATION OF PROTOTYPING METHODS AND THEIR CONTRIBUTIONS TO DESIGN KNOWLEDGE," *Proceedings of the Design Society,* vol. 1, pp. 1303-1312, 2021, doi: 10.1017/pds.2021.130.

[9] H. T. Rostami, M. F. Najafabadi, and D. D. Ganji, "Investigation of tire stiffness and damping coefficients effects on automobile suspension system," *Proceedings of the Institution of Mechanical Engineers, Part D: Journal of Automobile Engineering,* vol. 237, no. 14, pp. 3313-3325, 2023/12/01 2023, doi: 10.1177/09544070231151860.

[10] C. K. Oldeide, "Carbon Fibre Wheels for Formula Student [NTNU]," 2014.

[11] K. Korntved, "Design and Analysis of a Formula Student Carbon Fibre Rim," 2014.

[12] N. Petrone and F. Giubilato, "Methods for evaluating the radial structural behaviour of racing bicycle wheels," *Procedia Engineering,* vol. 13, pp. 88-93, 2011/01/01/ 2011, doi: https://doi.org/10.1016/j.proeng.2011.05.056.

[13] C. F. Heddleson, "Summary of Drag Coefficients of Various Shaped Cylinders," 1957.

[14] C. UK, "Mould Tooling For Fibre Reinforced Polymer Composites," 2023. [Online]. Available: https://compositesuk.co.uk/wp-content/uploads/GPG/Mould-Tooling-for-Fibre-Reinforced-Polymer-Composites.pdf?utm_source=chatgpt.com